The role of microstructural characteristics of additively manufactured Alloy 718 on tool wear in machining

International Journal of Machine Tools & Manufacture 171 (2021) 103814

Contents lists available at ScienceDirect

International Journal of Machine Tools and Manufacture

journal homepage: www.elsevier.com/locate/ijmactool

The role of microstructural characteristics of additively manufactured Alloy 718 on tool wear in machining

Amir Malakizadi [a,*], Tina Hajali [a], Fiona Schulz [a], Stefan Cedergren [b], Joakim Ålgårdh [c], Rachid M'Saoubi [d,e], Eduard Hryha [a], Peter Krajnik [a]

[a] Division of Materials and Manufacture, Department of Industrial and Materials Science, Chalmers University of Technology, Göteborg, SE-412 96, Sweden
[b] GKN Aerospace Engine System, Research and Technology Centre, 461 81, Trollhättan, Sweden
[c] GE Additive | Arcam EBM, Designvägen 2, 43533, Mölnlycke, Sweden
[d] R&D Material and Technology Development, Seco Tools AB, 737 82, Fagersta, Sweden
[e] Division of Production and Materials Engineering, Department of Mechanical Engineering Sciences, Lund University, Naturvetarvägen 18, 223 62, Lund, Sweden

ARTICLE INFO

Keywords:
Additive manufacturing
Powder bed fusion
Machining
Tool wear
Alloy 718

ABSTRACT

This study aims to provide a fundamental understanding of the role of microstructural characteristics influencing tool wear when machining Alloy 718 fabricated using Powder Bed Fusion (PBF). The effects of preferred crystallographic orientation (texture), shape and distribution of grains, local misorientation, type and amount of precipitates as well as the type, size and amount of abrasive carbides, nitrides and oxides on tool wear are investigated in as-built condition and after the standard solutionising and double-aging treatment. The microstructures of workpiece materials and the surfaces of worn tools were examined using different material characterisation techniques, including Scanning Electron Microscopy (SEM), energy-dispersive X-ray spectroscopy (EDS) and electron backscatter diffraction (EBSD). A dislocation-based approach was used to reveal the cumulative effects of the microstructural characteristics on deformation behaviour and the thermo-mechanical loads on the tools during cutting. The analyses suggest that texture and the extent of material work-hardening prior to the onset of crack formation markedly influence the amount of plastic work and thus heat generation when machining Electron Beam Powder Bed Fusion (EB-PBF) material. The higher heat generation in the cutting zones provokes thermally-induced wear mechanisms like diffusion-dissolution and oxidation. In addition, the larger amount of hard oxide inclusions present in EB-PBF material leads to higher wear by abrasion. In contrast to the prevailing experimental approaches in this field, the present investigation is built on a physics-based framework to understand the fundamental aspects that govern material deformation and heat generation in cutting and, consequently, tool wear mechanisms. This framework can be used for machinability assessment of any alloy manufactured by different additive manufacturing (AM) technologies and for optimising the process-chain, including printing strategies and thermal post-treatments, to improve the machinability of AM alloys by tailoring their microstructure.

1. Introduction

Alloy 718 – also commonly known as Inconel® 718 – is a Nickel–Iron-based superalloy widely used for fabrication of advanced components where high temperature strength (up to 700 °C) and high-temperature creep and oxidation resistance are required [1]. These properties make this alloy an excellent choice for manufacturing critical components of aero-engines, gas turbines and nuclear reactors. However, Alloy 718 is regarded as a difficult-to-cut material, partly because of its superior high temperature properties [2–5].

The machinability of the wrought and as-cast Alloy 718 has been addressed in numerous studies. Many studies focused on understanding of the tool wear mechanisms when machining Alloy 718 using different tool materials and under various cutting conditions. Bhatt et al. [2] investigated the wear mechanisms of uncoated WC-Co and PVD-TiAlN- and multi-layer CVD-TiCN/Al_2O_3/TiN-coated WC-Co tools when machining Alloy 718. They reported abrasion and adhesion as the main wear mechanisms. The coatings improved the tool wear-resistance at higher cutting speeds, whereas uncoated tools outperformed the coated

* Corresponding author.
E-mail address: amir.malakizadi@chalmers.se (A. Malakizadi).

https://doi.org/10.1016/j.ijmachtools.2021.103814
Received 31 July 2021; Received in revised form 6 October 2021; Accepted 7 October 2021
Available online 11 October 2021

tools at cutting speeds below 50 m/min. Grzesik et al. [6] investigated the wear mechanisms of AlTiN- and TiAlN-coated WC-Co tools. Similarly, the authors reported abrasion and adhesion as the dominant wear mechanisms. Bushlya et al. [7] studied the performance of ceramic and cBN tools when machining Alloy 718. The thermally induced mechanisms (diffusion) were shown to be dominant for the Whisker-reinforced alumina ceramic tools, whereas abrasion was identified as the main wear mechanism for the cBN tools. However, a recent investigation showed that thermally activated mechanisms like diffusion and oxidation would play dominant roles for cBN tools, depending on the binder composition and the range of cutting conditions [8]. A number of studies placed their focus on enhancing tool performance (tool life) by improving the tribological conditions at the tool-chip and tool-workpiece interfaces. Application of textured tools [5,9,10] and utilisation of high-pressure cooling [11,12], cryogenic cooling [13,14], MQL [13,15], ultrasonic vibration-assisted machining [16] and laser-assisted machining [17] were among those attempts. Several studies investigated the effects of microstructural properties on tool wear when machining Alloy 718. For example, Cedergren et al. [18] investigated the effects of grain size on notch wear. The authors observed that the material grain size has a large impact on notch wear formation. Olovsjö et al. [19] reported a strong correlation between flank wear rate and material hardness, while grain size had the largest effect on notch wear formation. Hoier et al. [3] investigated the amount and size-distribution of the carbo-nitrides in Alloy 718 and Waspaloy. Abrasion was identified as the main cause of the higher flank wear-rates observed when machining Alloy 718. Similarly, Furusho et al. [20] identified abrasion by MC carbides as the main wear mechanism for cemented carbide tools and modified the composition of Alloy 718 to reduce the amount of those precipitates. They observed significant improvements in the machinability of the modified Alloy 718 within the range of cutting conditions where mechanically-induced mechanisms played major roles. Olovsjö et al. [21] and Avdovic et al. [22] developed a methodology to evaluate the machinability of Alloy 718 based on its micro- and macro-properties like abrasiveness, ductility, strain hardening, thermal conductivity and hardness. These investigations identified carbon content [21,22] and variations in Al, Ni, Mn and Cr, grain size and hardness [21] as the major factors influencing the machinability of Alloy 718.

For the manufacturing of highly complex aero-engine components, additive manufacturing (AM) has gained increasing importance in recent years and partly replaced conventional manufacturing processes such as casting and forging. One of the technology's unique advantages is offering redesign opportunities through its layer-by-layer manufacturing process, which can result in considerable weight reduction. As a near-net-shape (NNS) process, it also enables substantial cost reduction associated with conventional machining processes [23]. In particular, powder-based AM technologies, which consolidate powder feedstock using laser or electron beams as the energy source, are of industrial relevance for manufacturing of advanced components [24,25].

The machinability of additively manufactured Alloy 718 has recently been addressed in several studies. Chen et al. [26] compared the machinability of wrought Alloy 718 and Laser Based Powder Bed Fusion (LB-PBF)-processed Alloy 718 using both coated and uncoated cemented carbides. The authors reported no major difference in tool wear when machining the two materials with the uncoated tool, whereas they observed a significantly improved tool life when machining the additively manufactured Alloy 718 when using the coated tool. Ducroux et al. [27] reported a 50% shorter tool life in milling of the wrought test pieces compared to the materials fabricated by LB-PBF technology. The abrasion and attrition were identified as the dominant wear mechanisms when machining the LB-PBF Alloy 718. Careri et al. [28] reported similar wear rates when machining Alloy 718 manufactured by Direct Energy Deposition (DED) compared to wrought or as-cast materials. As in other investigations, abrasion and adhesion were identified as the main wear mechanisms. The results of these studies suggest that the tool wear behaviour when machining additively manufactured alloys largely depends on the fabrication method and properties of the material being machined.

Hosseini and Popovich [29] summarised the hardness and tensile properties of Alloy 718 fabricated by various AM technologies and by conventional methods, such casting and forming. Their analyses showed a rather large scatter in hardness and tensile properties of the AM materials. For example, in as-built condition, the ultimate tensile strength (UTS) of materials fabricated by LB-PBF is in the range of 750–1200 MPa, whereas for materials manufactured by EB-PBF (Electron Beam Powder Bed Fusion) the range is less: 900–1200 MPa. A large scatter was also observed in tensile properties of heat-treated materials. The variations in the tensile properties of the wrought material were slightly narrower. This points to the dominant role played by microstructural characteristics on the mechanical properties of AM fabricated components – such as texture; grain size distribution; number and type of AM-specific defects (e.g. lack of fusion porosity, oxide inclusions, etc.); and the amount of precipitates. These characteristics vary with the AM technology, geometry of the fabricated parts, and the printing strategies and parameters [29]. In view of the methodologies presented by Olovsjö et al. [21] and Avdovic et al. [22], this data-driven observation based solely on hardness and tensile properties [29] does not provide clear conclusions regarding the so-called "cutting resistance" and expected tool wear behaviour when machining additively manufactured Alloy 718.

In contrast to the prevailing experimental and statistical approaches for machinability assessment explored above, this study aims to provide a fundamental physics-based understanding of the role of microstructural characteristics on tool wear when machining additively manufactured Alloy 718. The focus lies on investigating material fabricated using LB-PBF and EB-PBF – while using wrought material as the reference point. Tool wear investigations are performed on both as-built (or as-received) material and heat-treated (solutionised and aged) material according to the AMS-5662 standard. Different characterisation tools including Scanning Electron Microscopy (SEM), energy-dispersive X-ray spectroscopy (EDS), and electron backscatter diffraction (EBSD) technique are used to examine the microstructures of workpiece materials and worn tool surfaces. A mechanism-based (dislocation-based) approach is used to investigate the effects of the following workpiece material microstructural characteristics on the thermo-mechanical loads exerted on the tool surfaces during metal cutting: a) preferred crystallographic orientation (texture), b) shape and distribution of grains, c) local misorientation, and d) type and amount of precipitates. As a result, this investigation advances the current understanding of the role of microstructural properties influencing the machinability of Alloy 718 and, therefore, enables tailored process-chain design for improving tool performance when machining additively manufactured components using different AM technologies.

2. Experimental

2.1. Workpiece materials

Workpiece materials fabricated by three different manufacturing processes were used in this investigation:

- Wrought workpieces (85 mm outer diameter, 23 mm inner diameter, 47 mm height) were extracted from a large disc using a waterjet. The cylindrical samples extracted from the centre were kept for metallographic analysis, described in Section 2.3.
- Four LB-PBF workpieces (outer diameter 78.5 mm, inner diameter 25 mm, height 47 mm) were fabricated using an EOS M290 LB-PBF machine equipped with a Yb-fibre laser (maximum nominal power 400 W). The standard parameters for Alloy 718 were used, with a 40 μm layer thickness (under the license name: IN718_PerformanceM291 2.11) consisting of an optimized sequence of in-fill and

contour scanning, with the latter ensuring dimensional accuracy and good surface properties. The process was performed under Ar (Argon 4.6) with the laser scanning rotated 67° between each layer. The process atmosphere is established by flushing the build chamber with the inert gas until a stable oxygen level of 0.1% O_2 is achieved [30].

- Three EB-PBF workpieces were fabricated using an ARCAM EBM Spectra H machine with a powder-bed temperature of 975 °C ± 25 °C and 4 × 10^{-9} bar oxygen partial pressure in the build chamber. Process parameters were experimental, but in accordance with the standard Arcam EBM IN718 4.2.72 theme with a layer thickness of 70 μm. The workpiece dimensions of the hollow cylinders were (outer diameter 77.0 mm, inner diameter 24.5 mm, height 47 mm).

One workpiece from each manufacturing process was heat treated according to the AMS-5662 standard designed for wrought Alloy 718 in a lab-based Nabertherm high-temperature furnace. The heat-treatment cycle included a solution treatment at 954 °C for 1 h followed by water quenching to room temperature. Aging treatment was performed at 718 °C for 8 h, followed by furnace cooling to 621 °C for 10 h and subsequent ambient-temperature cooling in air.

2.2. Machining tests

Tool-life tests were carried out on an EMCO TURN 365 CNC lathe under the following cutting conditions, based on the tool manufacturer's recommendations for finish machining: cutting speed 40 m/min, feed rate 0.12 mm/rev, depth of cut 0.4 mm. The workpieces were face-turned using CNMG 120404-MF1 uncoated WC-Co inserts (Seco grade 890 – edge radii ≈ 25 μm), mounted on a DCLNR2525X12JETI holder (Fig. 1) with −6° orthogonal rake angle, −6° inclination angle, and 95° entering angle. This holder is equipped with an integrated coolant clamp that provides precision flow of metalworking fluid towards the cutting edge. The coolant (5.5–6.5% emulsion, 6–8 bar inlet pressure) was supplied to both the rake and flank surfaces of the inserts using the coolant clamp and the internal cooling channels. The cutting forces were measured using the Kistler 9257 A three-component dynamometer. Fig. 1a shows the machining set-up. The outer surfaces of the additively manufactured workpieces were machined (~1 mm depth) prior to the tool life tests to eliminate the effects of microstructural gradients close to the surface.

The cutting edges were examined after each machining pass using a stereo-optical microscope (Zeiss Discovery V20) to measure both flank and notch wear developments. One pass is equivalent to one complete cut of 0.4 mm machining depth from the workpiece outer diameter to inner diameter. The ISO 3685:1993-compliant tool life tests were stopped when either of the following criteria was met: a) maximum flank wear land width (VB_{Bmax}) of 0.2 mm, b) notch wear width (VB_N) of 0.3 mm, or c) chipping on the cutting edge. Additionally, in cases where a slow wear evolution was observed, the tool-life tests were terminated after the tenth machining pass, equivalent to 4 mm of total axial depth. In most cases, the tool-life tests were performed one time under the given cutting condition – restricted by the availability of additively manufactured materials. Therefore, the wear evolution and cutting-force measurements were only presented for those inserts which were characterized in depth.

2.3. Workpiece and tool wear characterisation

The workpieces and tools were examined using a LEO 1550 Gemini scanning electron microscope (SEM) equipped with an Oxford X-Max silicon drift detector for performing energy-dispersive X-ray spectroscopy (EDS). Imaging was performed using both secondary electrons (SE) and backscattered electrons (BSE). Two rings of approximately 10 mm thickness were sliced from the bottom and top surfaces of one of the LB-PBF and EB-PBF workpieces, as shown in Fig. 1b. The metallographic samples were then extracted from these rings to examine the microstructural variations in both build-direction (S1 surface, Fig. 1b) and perpendicular to the build-direction on the scanned surface (S2 surface, Fig. 1b). For the wrought material, metallographic samples were prepared from the cylinders taken from the centre of the workpieces. A Zeiss light optical microscope (LOM) and image-processing software ImageJ were used to measure the amount and size of carbides, nitrides and oxides within the workpiece materials on the mechanically polished samples prior to chemical etching. The type (composition) of these micro-constituents was determined using EDS after image analysis. The Vickers hardness of the materials was obtained using a Struers DuraScan-70 G5 automatic tester on an equally spaced grid with 10 kg force (HV10), obtaining average values and standard deviations. All these analyses were performed across the entire S1 surface parallel to the build direction, as shown in Fig. 1b, and on both samples extracted from bottom and top rings following ASTM E45 standard procedure. The samples were then etched using Oxalic acid (10 g/100 ml water) and waterless Kalling's No 2 reagent to obtain detailed analysis of other phases and for grain size measurements using ASTM E112 and ASTM E92 standard procedures. In cases where the grain boundaries were not revealed by chemical etching, electron backscatter diffraction (EBSD) was used to obtain the grain size distributions. An HKL Nordlys EBSD detector (Oxford Instruments) was used for EBSD analysis. Additionally, crystallographic texture and local grain misorientations – kernel average misorientation (KAM) – were examined on the finely polished surfaces prepared using 0.04 μm colloidal silica as the final polishing step. MTEX (V5.7.0) MATLAB-based free texture analysis toolbox was used. Here, both S1 and S2 surfaces (parallel and perpendicular to the build direction) of the sample taken from the top ring were examined under 20 kV accelerating voltage using a 2 μm step-size while a 10° threshold was used for grain boundary identification. Step-sizes of

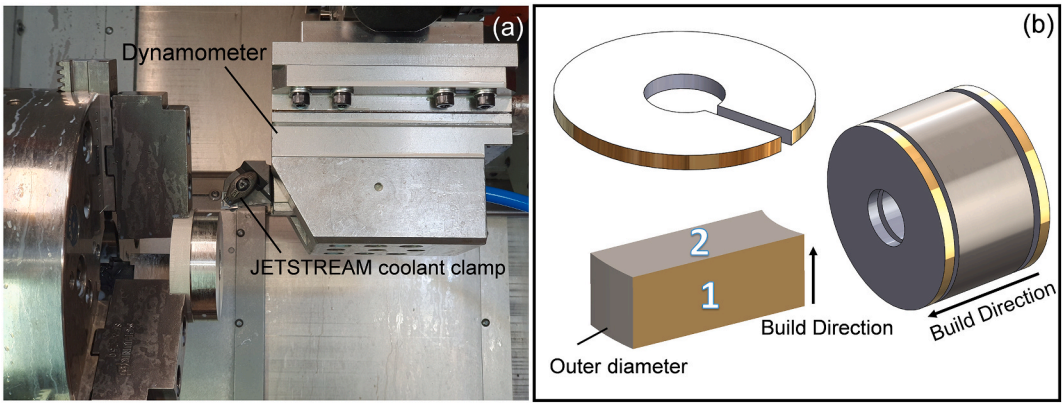

Fig. 1. The machining set-up (a), and the sample preparation for microstructural analysis (b).

1 μm and 0.25 μm were also used in a few cases to re-assess the KAM estimations at higher magnifications. However, no noticeable difference was observed in intensity or the general trends and thus those examinations are not reported. The worn tools were characterized using SEM both directly after the tests and after removal of adhered workpiece material using a diluted HCl solution. All inserts were etched for the same duration.

3. Results

In order to explain the tool wear observations and determine the dominant wear mechanisms when machining wrought, LB-PBF and EB-PBF materials, the microstructure of the workpieces was investigated in more detail on surfaces parallel and perpendicular to the rolling and build directions (RD and BD, respectively). The microstructural investigations of the AM material presented here should be regarded as general observations (on average) within and across the workpieces.

3.1. Texture and grain size distribution

The microstructure of the additively manufactured workpieces was examined in both build direction (S1 surface, Fig. 1b) and perpendicular to the build direction on the scanned surface (S2 surface, Fig. 1b). In the case of wrought material, the preliminary analysis using LOM suggested that grain size distribution is nearly similar both along and perpendicular to RD. Therefore, detailed microstructure examination was conducted solely on the surface parallel to RD. Here, the kernel density estimator was used to calculate the orientation distribution function (ODF), and the Kullback-Leibler cross validation (KLCV) was used for the optimal kernel estimation. The results are presented in the inverse pole figures, indicating the density of specific crystallographic orientations in BD and transverse direction (on S1 surface, Fig. 1b).

The material fabricated using EB-PBF consists of columnar grains – aligned along BD – and colonies of equiaxed grains with smaller sizes. This mixed distribution of grains was reported by several authors [31,32]. Studies show that the parameters such as spot time, beam current and line offset can affect the cooling rate and therefore the microstructure development in the EB-PBF process [29,33]. The columnar grains in the as-built material showed a strong texture in [001]//BD as shown in Fig. 2a. The LB-PBF samples showed a weak texture in [011]//BD and a relatively stronger texture in [001]//TD (Fig. 2b). Several studies showed that the $< 100 >$ corresponds to the easy growth directions in materials with a face-centred cubic (FCC) crystal structure, e.g. austenitic stainless steels and nickel-based superalloys [24]. This preferential growth direction follows the temperature gradient during solidification. As a result, the grain morphologies and texture are affected by the process parameters such as the scanning strategy and the volumetric energy density [24]. For example, whereas several studies on LB-PBF-fabricated Alloy 718 reported a strong [001]//BD texture [29], Jiang et al. [34] and Wan et al. [35] observed texture in both [001] and [011] directions along the build and transverse directions depending on the process parameters. The wrought material in as-received condition consisted of equiaxed grains with a weak texture in [−111]//RD and [011]//TD (Fig. 2c). The solutionising and aging treatment did not change the dominance of preferred crystallographic orientations observed in the as-build/as-received materials as shown in Fig. 3. The wrought material contains a large density of twin boundaries (Primary Σ3: $< 111 >/60°$), as shown in Fig. 4a. The EB-PBF sample also comprises a small fraction of Σ3 twin boundaries, mostly confined in the regions containing equiaxed grains. In contrast, the density of twin boundaries in the LB-PBF sample is insignificant. A rather large density of annealing twins in LB-PBF-fabricated Alloy 718 is reported in several studies – however, mostly after homogenisation treatment at temperatures above 1050 °C [36,37].

In order to assess the grain size distribution of wrought and EB-PBF materials, the twin grains were merged (Fig. 4b). The grain size distributions are presented in terms of minimum and maximum feret diameters due to the presence of elongated grains with irregular shapes, particularly in the LB-PBF and EB-PBF materials, shown in Fig. 5. The histograms included the feret diameters within the 0–0.1 mm size span, since the density of large grains in EB-PBF and LB-PBF was significantly smaller, as can be seen in Figs. 2 and 3. The relative probability associated with the histogram plot is presented in such a manner that the sum of the bar heights within the entire range of feret diameters is less than or equal to 1.

The probability density function obtained using kernel distribution over the entire range of feret diameters is also presented in Fig. 5. These probability distributions were used to calculate the mean and median of the minimum and maximum feret diameter of the grains in wrought, LB-PBF and EB-PBF materials, on both S1 (parallel to BD) and S2 (perpendicular to BD) surfaces, shown in Table 1. In general, the smaller grains were observed on the S2 surface for both EB-PBF and LB-PBF materials, as shown in Fig. 6. The EB-PBF material contained predominantly equiaxed grains on the S2 surface, whereas the LB-PBF material contained a combination of round and elongated grains with high aspect ratios. This is evident from the colour code in Fig. 6, where the roundness factor for each grain is calculated based on the difference between maximum and minimum feret diameters:

$$Roundness\ factor = (Feret_{Max} - Feret_{Min}) / Feret_{Max} \quad (1)$$

As the roundness factor becomes larger, the observed aspect ratio also becomes larger, as shown in Fig. 6. The mean and median of the minimum and maximum feret diameters of the grains calculated on the S1 and S2 surfaces before and after solutionising and aging treatment

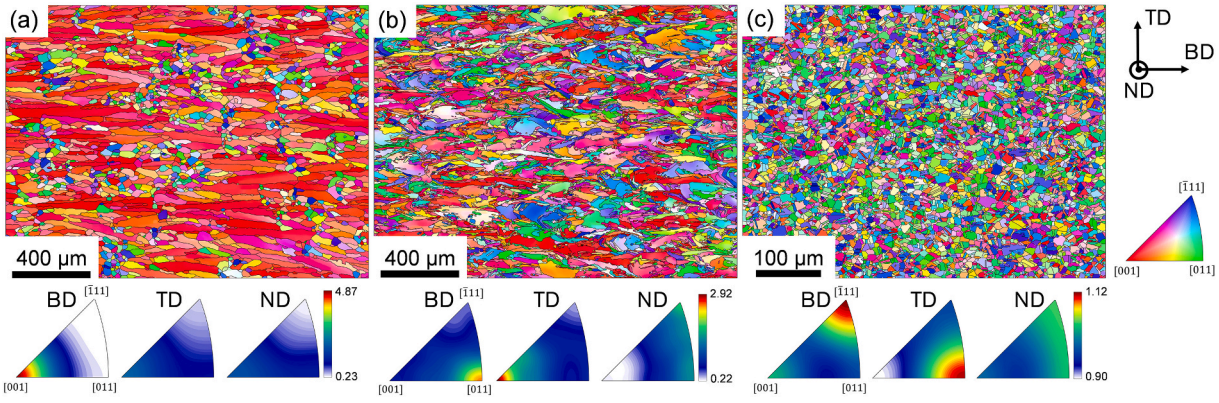

Fig. 2. EBSD inverse pole figure maps of EB-PBF (a), LB-PBF (b), and wrought (c) materials in as-built and as-received conditions. Build and transverse directions are designated as BD and TD, respectively. The inverse-orientation-distribution-function (ODF) plots are also shown below each case.

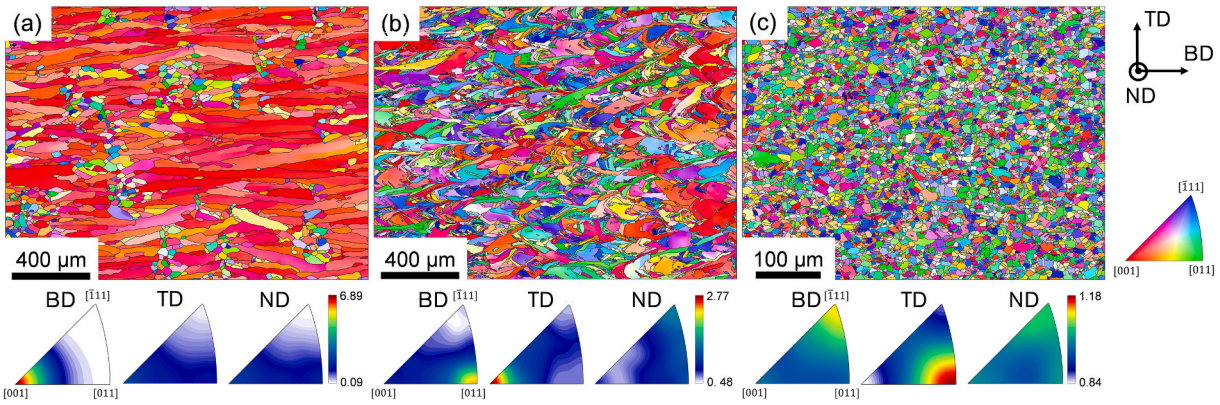

Fig. 3. EBSD inverse pole figure maps of EB-PBF (a), LB-PBF (b), and wrought (c) materials after solutioning and aging treatment. Build and transverse directions are designated as BD and TD, respectively. The inverse-orientation-distribution-function (ODF) plots are also shown below each case.

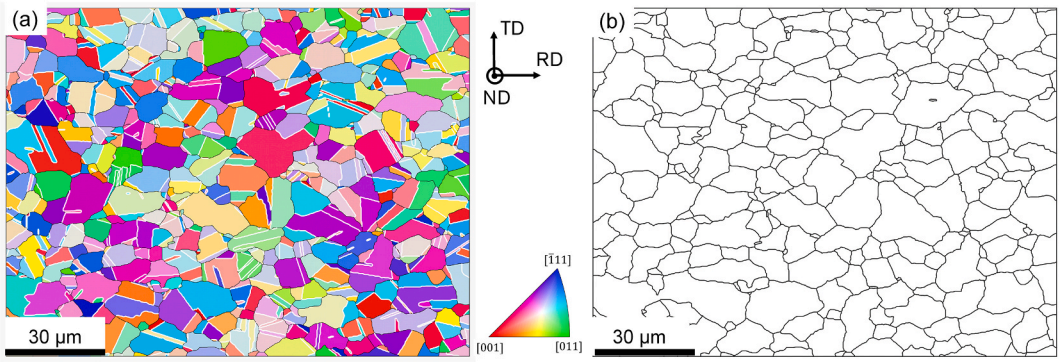

Fig. 4. Twin boundaries present in the wrought material (white lines) (a), and grain reconstruction after merging the twin grains (b). RD refers to rolling direction.

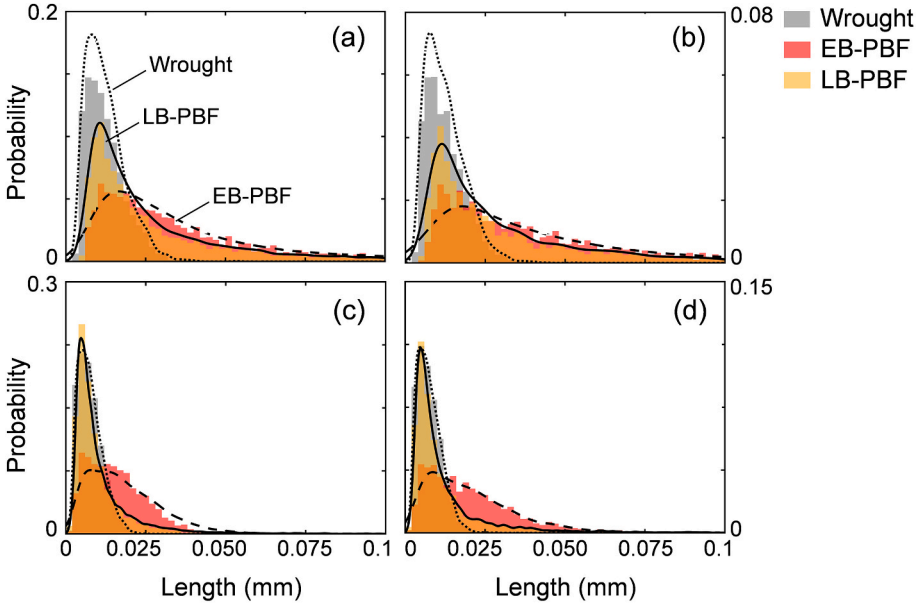

Fig. 5. Maximum feret diameter of grains in as-built/as-received conditions (a), after solutioning and aging treatment (b), Minimum feret diameter of grains in as-built/as-received conditions (c), and after solutioning and aging treatment (d), in wrought, EB-PBF and LB-PBF workpieces in the build direction - S1 surface (with reference to Figs. 2 and 3 after excluding the twin boundaries). The left axis is the normalised probability density of raw data (with 2 μm bin-width), whereas the right axis presents the probability based on kernel density estimator fitted over the entire range of minimum and maximum feret diameters (solid and dotted lines).

showed specific trends when comparing the microstructure of LB-PBF and EB-PBF workpieces (Table 1). EB-PBF material had a larger grain size on both S1 and S2 surfaces compared with that of LB-PBF material. The results, shown in Table 1, suggest that the solutionising and aging treatment has a large effect on grain size distribution on the S1 surface (parallel to build direction). However, further examination using BSE detector on the etched samples over large fields did not confirm such large differences in the grain size distribution before and after solutionising and aging treatments: only a minor difference was observed. This is expected, as the δ phase precipitated during the AM process at the grain boundaries is known to have a pinning effect at the temperature range used in this investigation for solutionising, inhibiting the grain

Table 1
The mean and median of the minimum and maximum feret diameter of grains in Wrought, LB-PBF and EB-PBF workpieces with reference to the EBSD data set presented in Figs. 2 and 3. The twin boundaries are excluded in the case of wrought and EB-PBF materials.

Material	Condition	Surface	Minimum feret diameter		Maximum feret diameter	
			Mean (μm)	Median (μm)	Mean (μm)	Median (μm)
LB-PBF	AB[a]	S1	10.7	7.4	31.4	19.1
		S2	14.6	11.4	27.3	21.1
	HT[b]	S1	12.2	7.7	35.6	21.5
		S2	11.0	8.0	21.0	14.9
EB-PBF	AB	S1	18.0	16.0	48.4	30.4
		S2	18.0	16.9	27.5	25.6
	HT	S1	20.1	17.3	63.5	35.9
		S2	19.8	18.3	29.8	27.4
Wrought	AR	S1	7.6	7.0	12.3	11.2
	HT	S1	7.6	7.0	12.5	11.3

[a] AB and AR stand for as-built and as-received conditions.
[b] HT stands for solutionised and aged condition.

growth. The wrought material had the smallest grain sizes among the three fabrication methods, and measurements (according to ASTM E112 standard) resulted in an average grain size of about 8 μm (ASTM number 11) before and after heat treatment. This value is in-line with the results presented in Table 1.

3.2. Misorientation

The kernel average misorientation (KAM) was calculated for the EB-PBF, LB-PBF and wrought samples. The KAM is a measure of local grain misorientation and represents the average of the disorientation angles between the pixel of interest and all its surrounding pixels in the EBSD map. Here, only the first-order neighbours were included in the KAM calculations. Additionally, a 3° threshold was applied to exclude the misorientations imposed by most sub-grain boundaries. Prior to KAM calculations, the EBSD maps were denoised using the half-quadratic minimisation algorithm [38] implemented in MTEX, with $\alpha = 0.5$. As seen in Fig. 7, the calculated misorientations were larger in the LB-PBF material in both as-built and heat-treated condition, whereas the EB-PBF and wrought materials indicated significantly smaller KAM values. This is believed to be due to the intrinsic differences between LB-PBF and EB-PBF fabrication processes. The temperature gradient in the vicinity of the beam is significantly larger during solidification in the LB-PBF

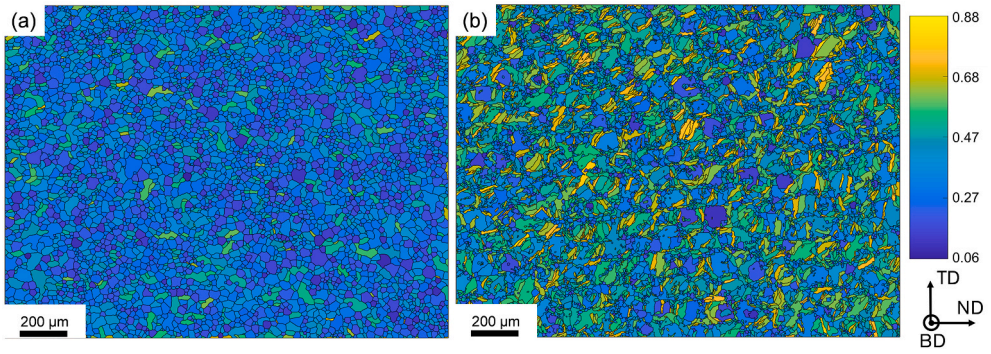

Fig. 6. Grain size distribution on S2 surface perpendicular to the build direction (BD) in EB-PBF (a), and LB-PBF (b) samples. The colour code represents the grain roundness calculated using minimum and maximum feret diameters (see Eq. (1)). (For interpretation of the references to colour in this figure legend, the reader is referred to the Web version of this article.)

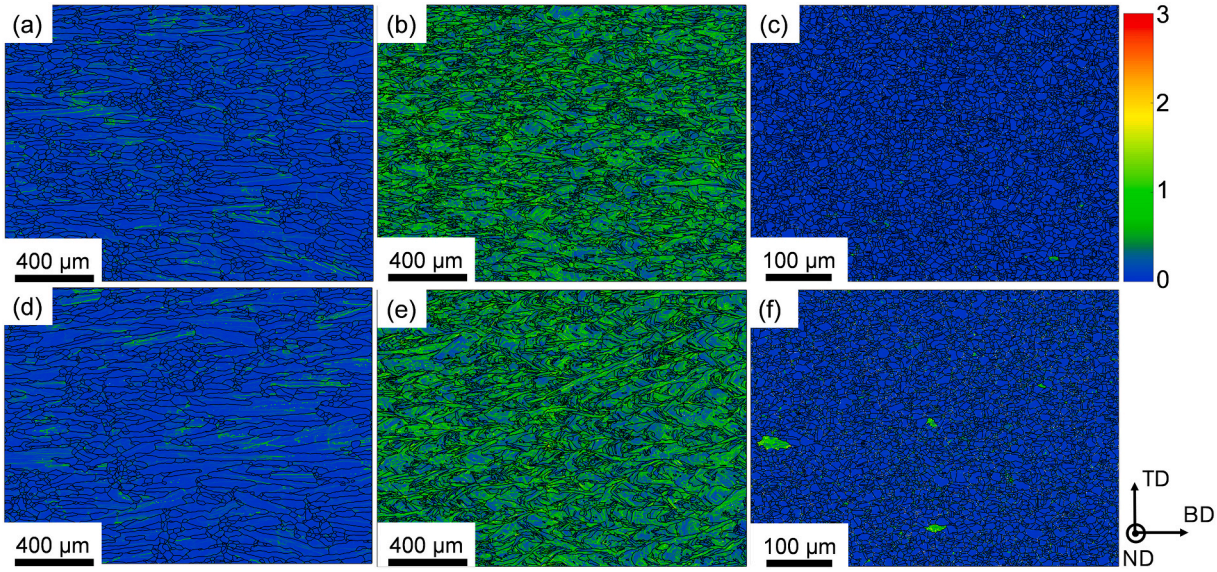

Fig. 7. Kernel Average Misorientation (KAM) of EB-PBF (a), LB-PBF (b), and wrought (c) workpieces in as-built or as-received conditions. Maps (d–f) represent the KAM estimations of the samples after solutionising and aging treatment.

process, which can lead to higher lattice curvature and thus larger misorientations [39]. The results presented in Fig. 7d–f shows no noticeable changes in misorientations after solutionising and aging treatment. The small misorientation in the wrought material implies an almost fully recrystalised microstructure in the as-received condition (Fig. 7c and f).

The normalised probability distribution of KAM calculations for the EB-PBF, LB-PBF and wrought materials are also shown in Fig. 8 for comparison. The results show a clear distinction between the materials. However, the heat-treatment did not have a notable effect on the misorientation. Fayed et al. [39] studied the effects of homogenisation and solution treatments of Alloy 718 fabricated by LB-PBF process. The authors reported a similar behaviour when exposing their material to a 2.5-h homogenisation treatment at 1080 °C.

3.3. Micro-constituents and hardness

3.3.1. Wrought workpieces

The wrought material consisted of δ-phase $Ni_3(Nb,Al)$ and (Nb,Ti) (C,N) carbo-nitrides as shown in Fig. 9. The EDS analysis indicated that these carbo-nitrides can well be classified as Ti-rich nitrides (or Ti-rich carbo-nitrides) and Nb-rich carbides (Fig. 10e and Fig. 10f). This enabled the determination of the amount of these micro-constituents by processing the images acquired using LOM prior to chemical etching [3]. The δ phase was randomly distributed within the grains and at the grain boundaries with a globular morphology. The globular δ phase forms when certain thermo-mechanical treatments are applied, as has been reported in several investigations [40,41]. The hardness measurements given in Fig. 11 suggested that the γ' and γ'' were not precipitated in the as-received condition. The average hardness of 274 ± 6.9 kg/mm^2 is well within the range for solution-treated materials with comparable grain size [19]. The average hardness increased to 434 ± 2.5 kg/mm^2 after heat treatment, indicating sufficient precipitation of γ' and γ'' to fulfil the minimum requirements set in the AMS-5662 standard. The average hardness value was comparable with the measurements presented by Cedergren et al. [18] and Olovsjö et al. [19] with comparable grain sizes. No notable gradient was observed in the hardness measured on S1 surface. Similarly, the morphology of the δ phase remained unchanged after heat treatment. Table 2 summarises the amounts of (Nb,Ti) (C,N) carbo-nitrides and their size in the investigated wrought material.

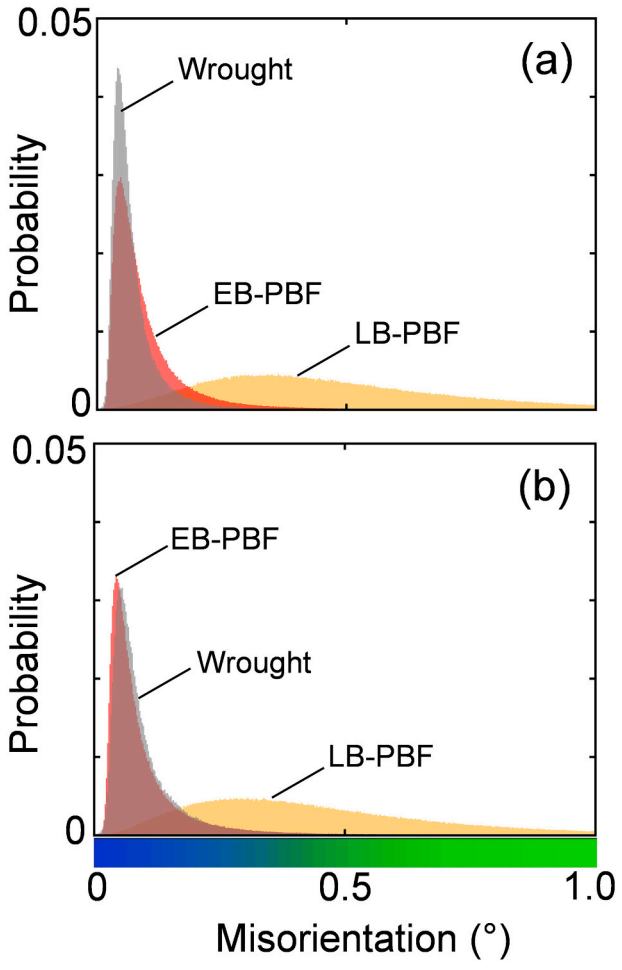

Fig. 8. Distribution of kernel average misorientation (KAM) of EB-PBF, LB-PBF and wrought workpieces in as-built and as-received conditions (a), and after solutionising and aging treatment (b). The colour bar represents the misorientation span with reference to Fig. 7. (For interpretation of the references to colour in this figure legend, the reader is referred to the Web version of this article.)

3.3.2. LB-PBF workpieces

The LB-PBF material in as-built condition primarily contained fine oxide inclusions and pores. EDS analysis indicated that the inclusions were mostly (Al,Ti)-rich oxides with an average size of about 9 μm^2 (examples given in Figs. 9h and 10d). Additionally, a fine distribution of Nb-rich phase was noted in the inter-dendritic regions, as shown in Fig. 9c. This phase is believed to be the Laves phase – $(Ni,Fe,Cr)_2(Nb,Mo,Ti)$ – which precipitates at the inter-dendritic regions due to micro-segregation of Nb, Ti and Mo during rapid solidification during the LB-PBF process [39,42]. The size and distribution of the oxide inclusions and pores remained unchanged during heat treatment. The Laves phase was largely dissolved during the solutionising step at 954 °C, and the needle-like δ phase precipitated both within the grains and along the grain boundaries (Fig. 9d). An accurate assessment of the amount and size-distribution of the oxide-inclusions was not possible using LOM image processing because the pores could not be differentiated from the oxides at low magnifications. Hence, Table 2 summarises the combined amount and size of both oxides inclusions and pores. The investigations at higher magnifications using SEM suggested that approximately 25–30% of those features identified in LOM were oxide inclusions. Precipitation of the γ' and γ'' was not expected in the as-built LB-PBF material [41]. The hardness measurements on the LB-PBF samples in as-built condition showed a higher average hardness than the wrought material in as-received condition. No difference in the measured hardness on the bottom and top samples was noticed (325 ± 4.95 kg/mm^2 and 327 ± 4.5 kg/mm^2, respectively). The average hardness of the LB-PBF samples after solutionising and double aging treatment surpassed the wrought and EB-PBF materials.

3.3.3. EB-PBF workpieces

The EB-PBF material in as-built condition contained δ phase precipitates, (Nb,Ti) (C, N) carbo-nitrides, oxide inclusions, and pores. The carbo-nitrides were often attached to the oxide inclusions (Fig. 9a) and could clearly be classified into Ti-rich nitrides (or Ti-rich carbo-nitrides) and Nb-rich carbides, although mixed compositions were also noted (Figs. 9h and 10b). The difference in compositions provided sufficient contrast in LOM and made it possible to determine the amount and size of these particles using image processing. The results are summarised in Table 2. The δ phase was mostly precipitated at the grain boundaries; however, intergranular globular precipitation of δ phase was also observed (Fig. 9a). The oxide inclusions were primarily Al_2O_3 or (Al, Mg)-rich oxides (Figs. 9h, 10a and 10c). The average hardness measured on the bottom and top samples showed a slight difference: 370 ± 7.7 kg/mm^2 and 402 ± 6.1 kg/mm^2, respectively. Detailed analyses in previous studies [43,44] using transmission electron microscopy (TEM) showed that both γ' and γ'' precipitate during EB-PBF since the material is kept at

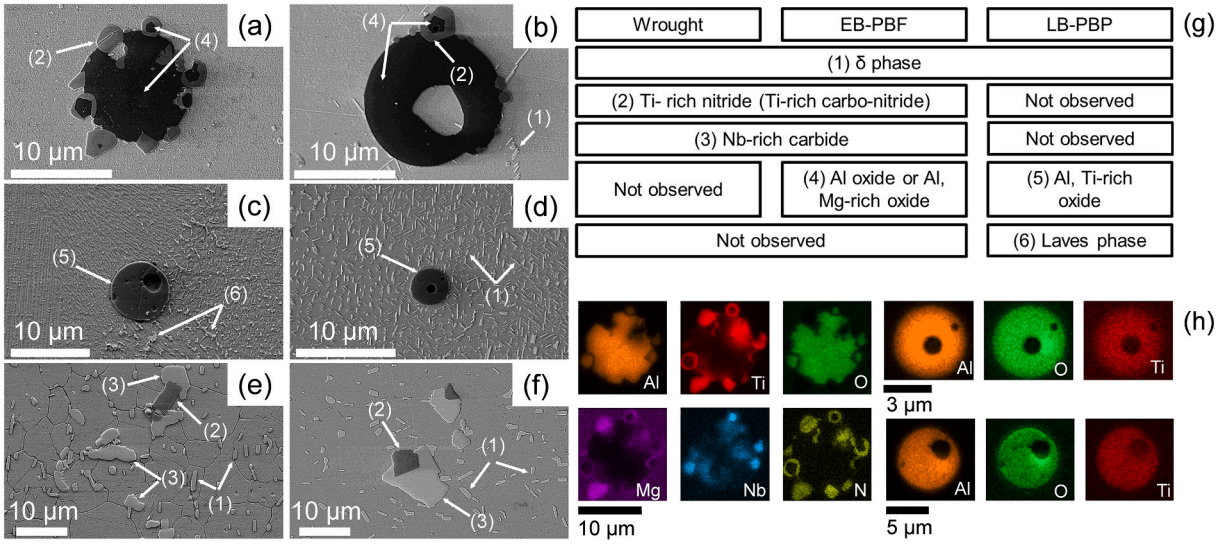

Fig. 9. Different types of micro-constituents in workpiece materials: EB-PBF (a), LB-PBF (c), and wrought (e) in as-built/as-received conditions; and EB-PBF (b), LB-PBF (d), and wrought (f) after heat treatment. The overall summary of the micro-constituent types observed in the workpiece materials (g). The numbered arrows in (a–f) refer to micro-constituents summarised in (g). The major elemental composition of the micro-constituents is shown in (a), (c) and (d), obtained using EDS with 20 kV accelerating voltage (h).

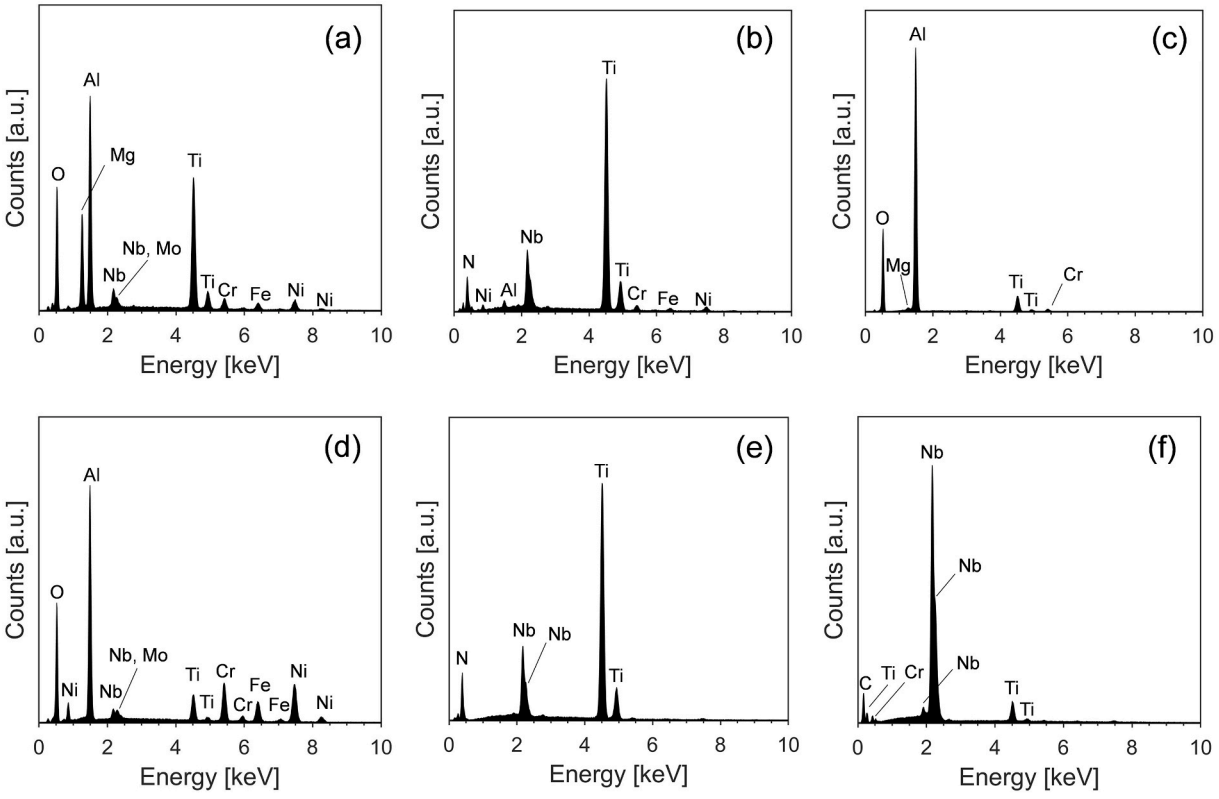

Fig. 10. EDS spectra of the various types of micro-constituents: type 4 in EB-PBF (a and c), type 2 in EB-PBF (b), type 5 in LB-PBF (d), types 2 and 3 in wrought material (e and f) measured with 20 kV accelerating voltage.

high temperature (975 °C ± 25 °C) during the entire manufacturing process and experiences slow cooling rates to room temperature. The partial precipitation of γ' and γ'' resulted in higher hardness than the wrought and LB-PBF samples in their as-received and as-built state, respectively. The average hardness values measured on the bottom and top samples reached to about 442 ± 8.7 kg/mm^2 and 439.6 ± 10.6 kg/mm^2, respectively, after heat treatment and the hardness gradient along the build direction was eliminated, as shown in Fig. 11. The grain boundaries after heat treatment contained a needle-like δ phase (Fig. 9b). No notable changes in the size and distribution of the oxide inclusions and carbo-nitrides were observed. The underlying deformation mechanisms resulting in different hardness of workpiece materials in as-received or as-built conditions and after heat treatment are discussed in Section 4.1.

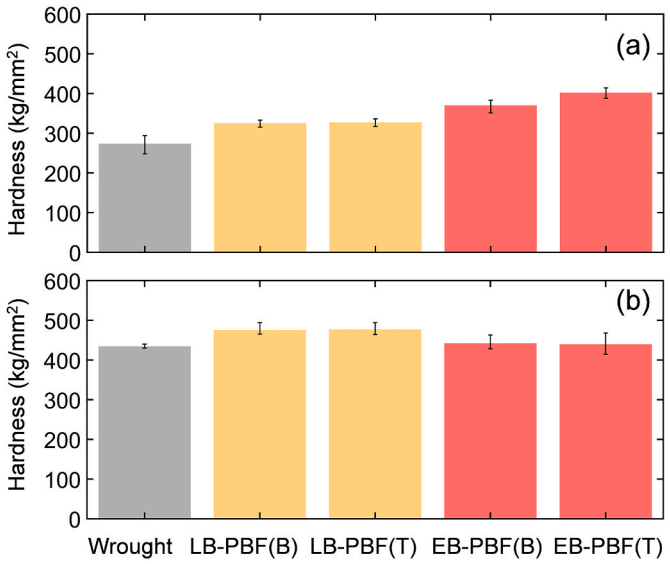

Fig. 11. Hardness of the wrought, LB-PBF and EB-PBF samples in as-built/as-received conditions (a), and after heat treatment (b). B and T refer to bottom and top samples. The measurements were performed on the S1 surface, shown in Fig. 1b. The error bars include the maximum and minimum recorded hardness values.

3.4. Cutting forces and tool wear

The cutting-force measurements when machining wrought, LB-PBF and EB-PBF material in as-received or as-built condition, and after the heat treatment using the fresh tools, are shown in Fig. 12. The results represent the average values in the beginning of the cut (the first 10 s of the first machining pass) to disregard the effects of wear development on the forces. Between the materials in as-built and as-received conditions, the highest cutting and feed forces were observed when machining EB-PBF material, whereas the forces were approximately the same when machining the LB-PBF and wrought workpieces. The cutting force was also highest when machining EB-PBF material after heat treatment, however, no notable difference between the feed and passive forces was observed in comparison to the wrought and LB-PBF material. All three force components were approximately the same when machining wrought and LB-PBF workpieces after heat treatment. Section 4.2 explores the reasons for these observations from a microstructural standpoint.

The results of tool-life tests, shown in Fig. 13, illustrate the evolution of flank and notch wear. Note that notch-wear measurements are presented for the major side of the cutting edge according to the ISO 3685:1993 standard. For the cases where notch wear was not observed, flank wear results were instead reported (Fig. 13 c-d). An overview of the worn edges at the end-of-tool-life tests is shown in Fig. 14. The tool life was shortest when machining the EB-PBF material; however, different wear modes were observed when machining the material in as-built condition and after solutionising and aging treatment. Notch wear was dominant when machining the material in the as-built condition, whereas a steady flank-wear progression was observed for the heat-treated workpiece – compare Fig. 14c and f. The rate of flank-wear evolution increased after solutionising and aging treatment. The LB-PBF material in as-built condition gave the slowest wear progression. However, the wear rate increased when machining the heat-treated workpiece. Notch wear was not observed for either material condition. The flank-wear progression rate when machining the wrought material only slightly changed after solutioning and aging treatment, however, the cutting edge was chipped out before the tool life criterion was met. The other notable observation is the presence of thick adhered material on the rake face of the tools and a relatively thinner layer on the flank surfaces, as shown in Fig. 14. The distinctive wear types when machining the materials fabricated using different manufacturing processes, as well as the effects of heat treatment on tool wear, are evident in this figure.

Fig. 15 shows the rake side of the tools after removal of the adhered materials using the HCl diluted etchant. Major chipping and fracturing on the rake face and near the cutting edges were observed in all cases except for machining LB-PBF after solutionising and aging treatment. An overview of the flank wear land after removal of the adhered material is shown in Fig. 16. As can be seen, large notch wear progression was also observed on the minor side of the cutting edge when machining wrought

Table 2
Summary of quantification of carbides, nitrides and oxides by image analysis.

Material	Average number of particles (per mm^2)			Average content (vol%)			Average and median of particle sizes (μm^2)[a]		
	TiN/TiCN	NbC	Oxides/pores	TiN	NbC	Oxides/pores	TiN/TiCN	NbC	Oxides/pores
Wrought	19	99	–	0.06	0.21	–	31(23)	21(11)	–
LB-PBF	–	–	38	–	–	0.03	–	–	9 (2.4)
EB-PBF	37	8	133	0.02	0.01	0.10	5(3.8)	11(9)	7(2.9)

[a] Median of particle size is given within parentheses.

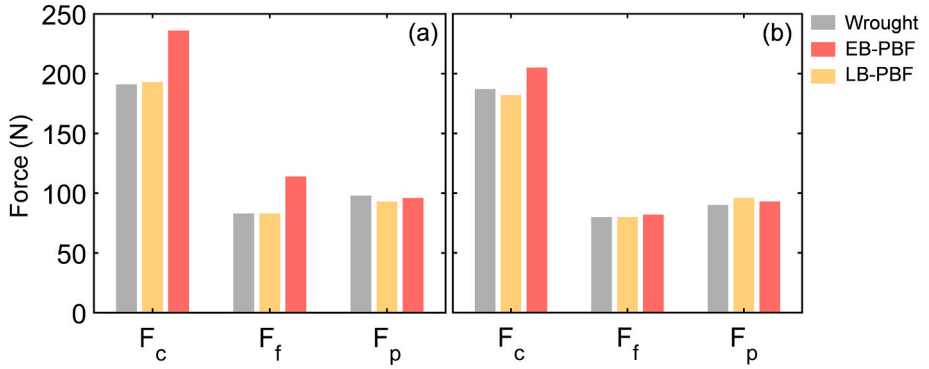

Fig. 12. Cutting (F_c), feed (F_f) and passive (F_p) forces measured when machining wrought, EB-PBF and LB-PBF materials in as-received and as-built conditions (a), and after solutionising and aging treatment (b). The results represent the measurements in the beginning of the tests (10 s) using a fresh tool.

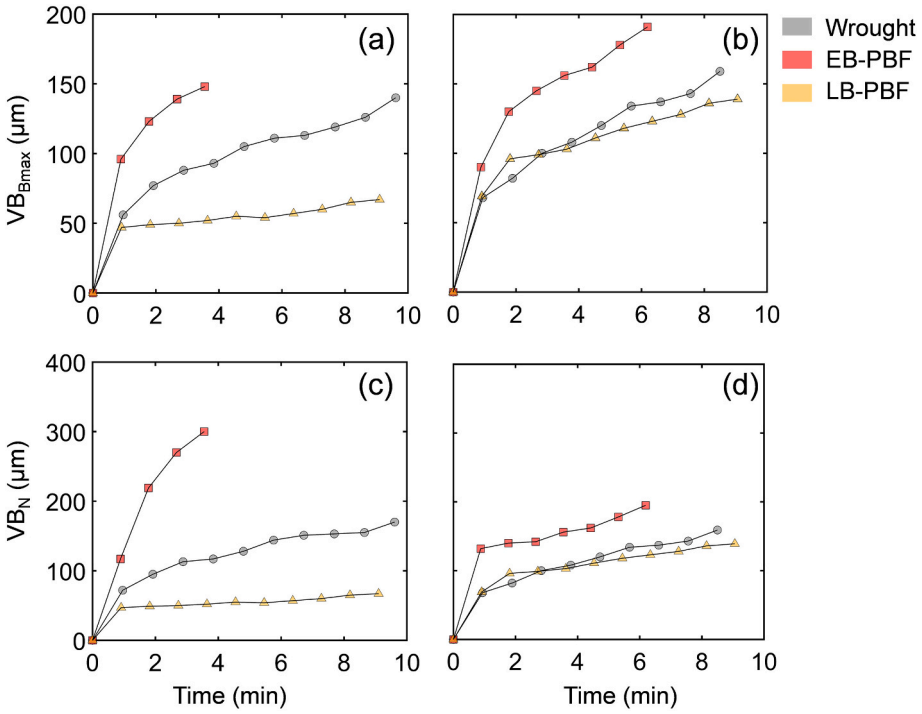

Fig. 13. Flank (VB_{Bmax}) and notch (VB_N) wear evolution when machining EB-PBF, LB-PBF and wrought materials in as-built and as-received conditions (a and c) and after solutionising and aging treatment (b and d).

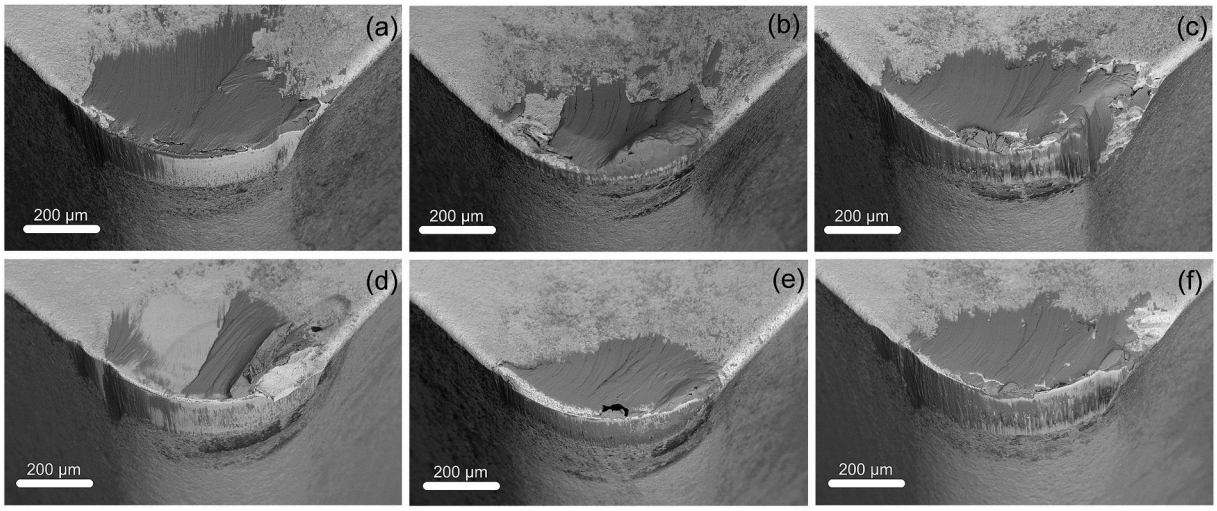

Fig. 14. Overview of the worn cutting edges when machining wrought (a and d), LB-PBF (b and e), and EB-PBF (c and f) materials in as-received or as-built conditions, and after solutionising and aging treatment, respectively.

and EB-PBF materials. However, the evolution of notch wear on the minor cutting edge was not monitored in this investigation as this wear type was not set as the tool-life criterion (see Section 2.2). The other notable observation was the presence of thin aluminium-rich oxide layers or fragments on the flank wear lands – which is identifiable as black and grey regions mostly where the wear land ends, as seen in Fig. 16. This was observed in all cases. However, their amount was higher when machining LB-PBF and EB-PBF materials. The oxides (and most ceramic materials) are nonresponsive to the diluted HCl solution and thus will not be dissolved. The fragmented aluminium-rich oxide layer on the flank wear land when machining LB-PBF material after solutionising and aging treatment is shown in Fig. 17. The detailed composition of this layer, obtained using EDS analysis, is also shown in this figure. This layer also consisted of small traces of Ni, Nb and Ti, which are likely associated with the residuals of built-up-layer (BUL) remained undissolved after HCl treatment. The EDS analysis showed no major indication of Ti or other elements in the oxide layers on the flank wear land when machining EB-PBF and wrought materials. In the case of EB-PBF and LB-PBF materials, this observation is in-line with the inclusion classification presented in Fig. 9, suggesting the oxide layer would form – as the oxide inclusions of the workpieces smear onto the flank wear land due to high temperatures and shear stresses. However, the formation of this oxide layer (or its fragments) would also stem from the oxidation of the γ phase or the aluminium-rich precipitates in the workpiece materials during the cutting process. This is inferred since the aluminium-rich oxide fragments were also observed when machining the wrought material (Fig. 16d), despite having no oxide inclusions identified in the workpiece material (Fig. 9g). Similar observations were

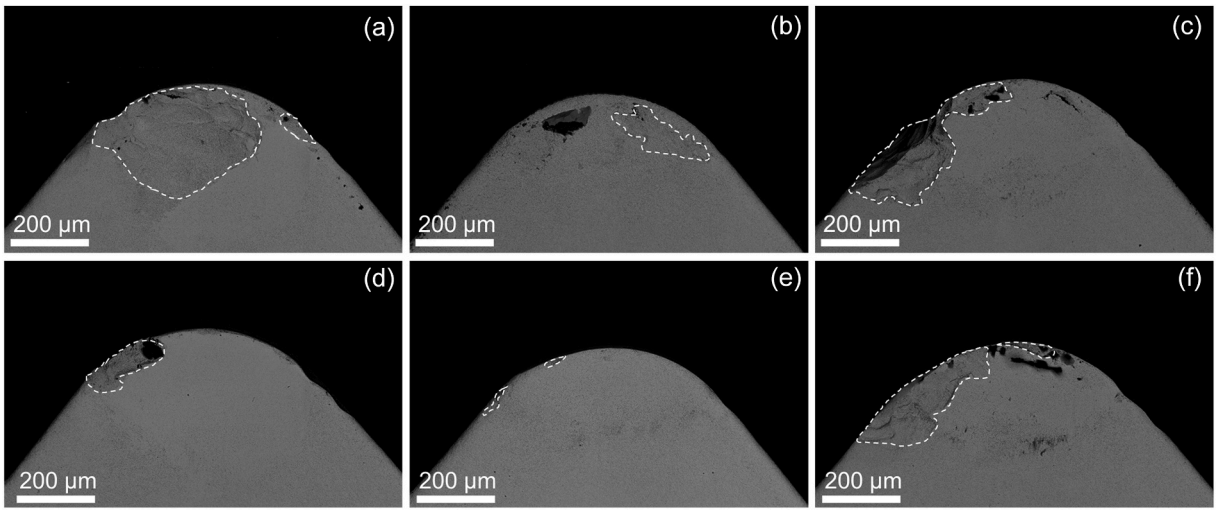

Fig. 15. Overview of the rake surface of the worn tools when machining wrought (a and d), LB-PBF (b and e), and EB-PBF (c and f) materials in as-received or as-built conditions, and after solutionising and aging treatment, respectively.

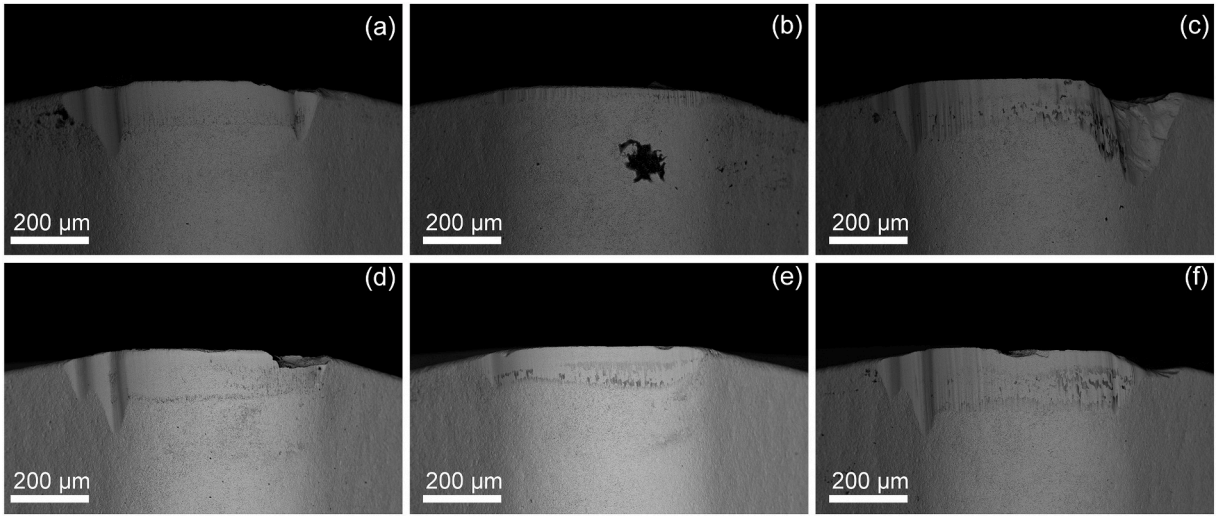

Fig. 16. Overview of the flank surfaces of the tools when machining wrought (a and d), LB-PBF (b and e), an EB-PBF (c and f) materials in as-received or as-built conditions, and after solutionising and aging treatment, respectively.

made by Hoier et al. [3] when machining wrought Alloy 718 using uncoated cemented-carbide tools. It should be stressed here that the amount of these oxide fragments was substantially lower when machining the wrought workpieces, as seen in Fig. 16, suggesting that the formation of the oxide layer (or its fragments) is likely a combination of the proposed effects that occurs during machining of LB-PBF and EB-PBF material. Fig. 18 shows the topography of the worn rake and flank surfaces after machining the wrought material, indicating that the WC grains were frequently pulled out on the rake and flank surfaces. After the adhered material was removed using HCl solution, it was seen that WC grains remained on the flank surface, as shown by the arrows in Fig. 18b.

4. Discussion

4.1. Microstructure effects on hardness

Hardness is considered one of the major parameters influencing tool wear when machining Alloy 718 [19,21,22]. The detailed microstructural investigation presented in Sections 3.1 to 3.3 showed a significant difference in terms of: a) grain size distribution; b) texture; c) misorientation (KAM); d) the amount of γ' and γ'' precipitates; and e) the type, amount and composition of oxides, nitrides, and carbides between the wrought, LB-PBF and EB-PBF materials in both as-received/as-built and heat-treated conditions. These microstructural characteristics have a significant effect on the yield-strength and flow-stress properties such as strain hardening, strain-rate hardening and thermal softening [45] as well as the energy dissipation during crack propagation [46]. The hardness is correlated with tensile strength properties as shown in a number of studies [47,48]. Hence, the hardness variations observed in the workpiece materials before and after heat treatment can be explained by exploring the effects of microstructural characteristics on tensile-strength properties.

Several studies have dealt with the prediction of flow-stress properties of Ni-based superalloys based on the underlying micro-mechanical mechanisms [45,49–51]. In these studies, it is generally assumed that the macroscopic flow stress of the material (σ_y) can be expressed in a cumulative manner as:

$$\sigma_y = \sigma_i + \sigma_{H-P} + \sigma_s + \sigma_p + \sigma_G + \ldots \quad (2)$$

where σ_i is the lattice friction stress (known as Peierls-Nabarro stress);

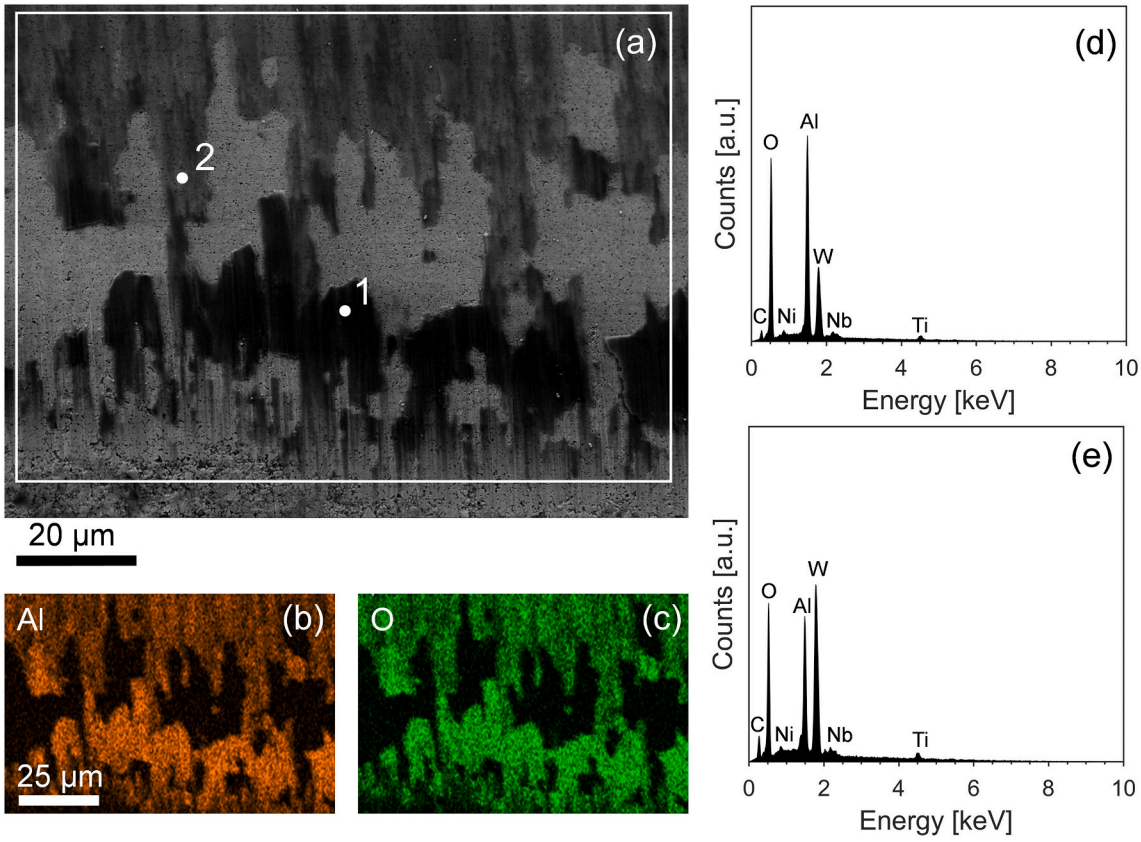

Fig. 17. Oxide layer observed on the flank wear land when machining LB-PBF material after solutioning and aging treatment with reference to Fig. 16e (a), EDS elemental maps of aluminium and oxygen (b and c), EDS spectra of point 1 (d) and point 2 (e), measured using 10 kV accelerating voltage.

σ_{H-P} is the stress contributions due to the Hall-Petch (H–P) effect (σ_{H-P} is inversely proportional to $\sqrt{D}$, where D is the average grain size); σ_s is the stress required to move dislocations in the presence of solute atoms (solid-solution strengthening effect); σ_p is the stress required to cut off or loop around a precipitate; and σ_G is the stress contribution associated with the long-range lattice disturbances of immobile dislocations. Complete descriptions of the dislocation-based (or microstructure-based) flow-stress models and the mathematical terms for the rate at which the dislocations are generated or annihilated based on different assumptions are given elsewhere [45,49,50]. The estimation of the flow stress of AM-fabricated and wrought materials requires a prior knowledge of the cooling history (e.g. to obtain the size and amounts of precipitates) and dedicated experiments. However, the effects of the microstructural characteristics can be explored in a qualitative manner, in view of their relative contributions to the different strengthening mechanisms given in Eq. (2).

The minimum and maximum feret diameters of the grains presented in Table 1 and Fig. 5 suggest that the contribution of the H–P effect (σ_{H-P}) would be largest for the wrought material with the smallest grain sizes, followed by the LB-PBF material. The smallest grain-boundary-strengthening effect would be expected for the EB-PBF material with the largest average grain size. However, a few studies [52–54] suggested that the preferred crystallographic orientation (texture) may influence the grain boundary strengthening mechanisms. Gokcekaya et al. [53] showed that the strongly textured Alloy 718 fabricated by LB-PBF demonstrated a reduced H–P effect on the yield strength in comparison to that of the untextured materials. On the contrary, Johnston and Feltner [54] argued that if the resolved shear stress on the slip planes of a specific grain is zero, it can act as a barrier to the dislocation glide (slip) in its adjacent grains. Hence, a substantial "*barrier hardening*" effect would be expected for a strongly textured material if such a relation holds between the slip planes of textured grains and the direction of the applied shear stress. Additionally, the low-angle grain boundaries and twin boundaries are believed to have large impacts on strain-hardening mechanisms and the overall strength of the materials [55].

A similar solid-solution strengthening effect (σ_s) would be expected for all investigated materials after solutionising and aging treatment (under the assumption that the temperature was sufficiently high and the holding time sufficiently long). The presence of the Laves phase in as-built LB-PBF material (Fig. 9c) indicates an uneven distribution of elements in the γ phase caused by large temperature gradients during printing. The Laves phase traps the solute atoms (Cr, Fe and Mo), and thus reduces the potential effects of those elements on solid-solution strengthening of the γ phase in Alloy 718. Hence, in the as-built condition, the solid-solution strengthening effect would be smallest for the LB-PBF material. The wrought and EB-PBF materials were expected to have a more homogenised γ phase in the as-received or as-built conditions since the materials were kept at high temperatures for sufficiently long times during manufacturing. The Laves phase in the as-built LB-PBF material was largely dissolved after solutionising and aging treatment and was replaced by a fine distribution of needle-like δ-phase, as shown in Fig. 9d. This suggests that the temperature and duration of the solutionising treatment were sufficient for the redistribution of atoms, and thus an approximately similar solid-solution strengthening effect as that of other materials would be expected.

The wrought and LB-PBF materials were expected to have limited or no precipitation of γ' and γ'' in as-received or as-built conditions, whereas these phases were partially precipitated in EB-PBF materials, as discussed in Section 3.3. Hence, the precipitation hardening effect (σ_p) would be limited for the LB-PBF and wrought materials in their as-built or as-received conditions while a rather large effect would be expected for EB-PBF material. However, the hardness gradient in the as-built EB-PBF material (see Fig. 11) suggests that there is a variation in type,

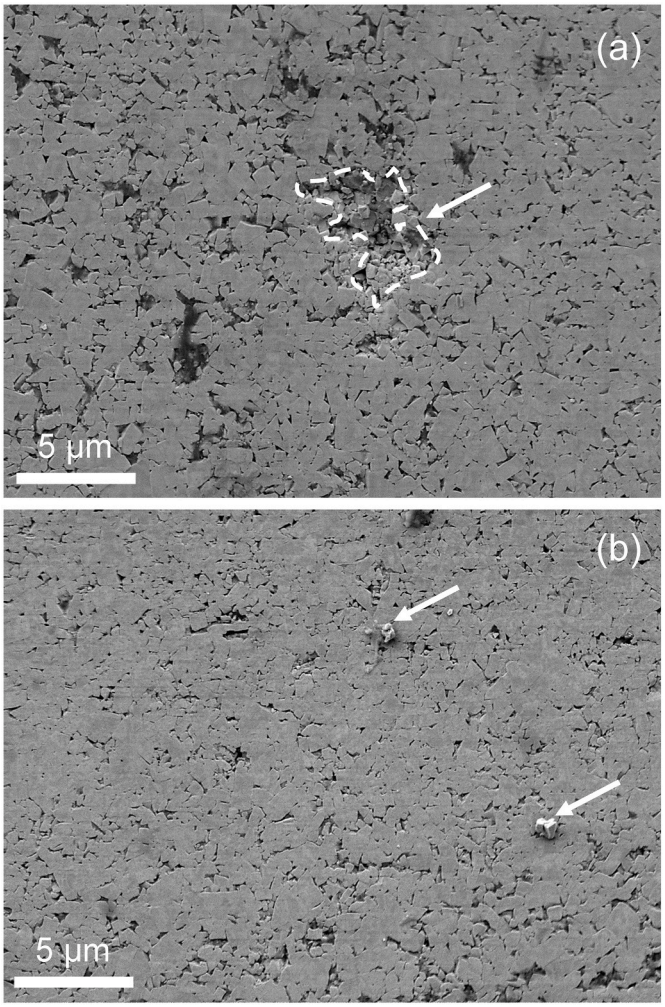

Fig. 18. Overview of worn surfaces on the tool rake (a) and flank (b) when machining wrought material after solutionising and aging treatment. SEM images taken after removal of the adhered layer using HCl solution. The WC grains were frequently pulled out and traces of them can be seen on the surfaces indicated by the arrows.

amount, size, shape and distribution of those precipitates within the material along the build direction. The stress required for the dislocations to bypass or bow around the precipitates depends on these parameters [45,51]. The hardness measurements suggested a sufficient precipitation of γ' and γ'' in the materials after heat treatment. Hence, approximately the same precipitation hardening effect would be expected in heat-treated materials.

The last term in Eq. (2) accounts for the stress contribution associated with the long-range lattice disturbances of immobile dislocations and can be described as:

$$\sigma_G = \alpha M G b \sqrt{\rho} \tag{3}$$

where α is a coefficient, M is the Taylor factor, G is the shear modulus, b is the Burgers vector of the dislocations, and ρ is the total immobile dislocation density within the material during deformation. Ashby [56] classified the dislocations into two types: geometrically-necessary dislocations (GNDs) and the statistically-stored dislocations (SSDs). The GNDs are stored to sustain the geometric continuity of the material during deformation, whereas the SSDs are the result of random incidents in the lattice during deformation. The density of GNDs (ρ_G) is proportional to the change in orientation between two adjacent indexed points and thus can be measured using EBSD analysis [57,58], whereas the density of SSDs (ρ_S) cannot be measured as they do not lead to an orientation gradient. The density of GNDs can be estimated from the Kernel Average Misorientation (KAM) measurements using the following relation [59,60]:

$$\rho_{GND} = \frac{\kappa \theta_{KAM}}{bs} \tag{4}$$

where κ is a constant varies between 2 and 4 for pure tilt or twist boundaries, respectively. b is the Burgers vector and s is the step-size of EBSD measurement. In this regard, KAM calculations presented in Figs. 7 and 8 suggest that the LB-PBF material has significantly larger density of GNDs compared to that of wrought and EB-PBF materials in both as-built and heat-treated conditions.

Based on these arguments, it is possible to explain the trends observed in the measured hardness values presented in Fig. 11 in a qualitative manner. The grain boundary (including twin boundaries) and solid-solution strengthening effects are the main mechanisms influencing the flow stress properties of the wrought material in as-received condition, thus the lowest hardness is observed in this material. The effect of grain boundary strengthening is lower for LB-PBF material (larger average grain size – see Fig. 5 and Table 1), but the crystal structure contained a large density of GNDs in the as-built condition. Hence, despite limited or no precipitation hardening, the hardness was larger than that of the wrought material. The grain-boundary strengthening effect is the least for the EB-PBF material due to the largest grain size, but the partial formation of γ' and γ'' provides some precipitation hardening effects. These resulted in the highest hardness for the EB-PBF material in the as-built condition. The precipitation of γ' and γ'' after solutionising and aging treatment adjusted the hardness values for all materials as expected. The LB-PBF material, with the additional effects of the largest density of GNDs, gave the highest hardness.

4.2. Microstructure effects on the thermo-mechanical loads in cutting

Experimental observations suggested that a major part of the plastic work($W = \int \sigma : d\varepsilon_p$ where σ and ε_p are the stress and plastic strain, respectively) transforms into heat (about 70–95%) [61,62]. Approximately 10–15% of the generated heat due to the plastic work in the primary and secondary shear zones transfers to the cutting tool [63,64], the amount of which depends on the thermal conductivity of the tool and workpiece materials and on the cutting and cooling-lubrication conditions [64]. This relatively small heat partitioning gives rise to a large temperature increase on the tool surfaces. A temperature range of 750–950 °C is reported when machining Alloy 718 at various cutting conditions using different tool materials [65,66]. This suggests that the thermally-activated mechanisms would have large impacts on tool wear evolution. In addition, high stresses exerted on tool surfaces would provoke different mechanically-induced wear mechanisms when machining Alloy 718. To this end, it is vital to investigate the influence of microstructural characteristics – specific to additive manufacturing processes – on deformation behaviour during machining and thus on the thermo-mechanical loads exerted on tool surfaces.

Among the as-built materials, the highest forces were observed when machining the EB-PBF workpiece. This material is believed to contain the largest amount of γ' and γ'' precipitates in the as-built condition, as mentioned in Section 3.3. Naturally, a higher precipitation-hardening effect is expected for this material. However, the forces when machining the as-built EB-PBF material – with only a partial precipitation of γ' and γ'' phases – were higher than all the heat-treated workpieces including the wrought and LB-PBF materials, as shown in Fig. 12. This observation is in agreement with the results reported by Hagberg and Malm [67], who investigated the material-deformation mechanisms when machining wrought Alloy 718. Higher cutting and feed forces were reported when machining the solutionised material in comparison

to the solutionised and aged material at the cutting speeds of 30 m/min and 60 m/min. Furthermore, higher forces were reported by the authors for the materials with larger grain sizes, regardless of whether they were solutionised or aged. These observations appear to be in contradiction with the cumulative effects of different strengthening mechanisms discussed in Section 4.1 (σ_p and σ_{H-P}). For example, the materials with larger amounts of precipitates and higher density of grain boundaries gave lower cutting forces during machining. Hence, there should be additional factors that can influence the so-called "cutting resistance" of the materials from the microstructural standpoint.

The mechanism-based, fundamental description of the flow stress behaviour, presented in Section 4.1, can be used to explain the experimental observations in cutting under certain considerations associated with the extreme thermo-mechanical loading conditions. The material deformation in metal cutting is very different from simple hardness or uniaxial tensile or compression tests. During cutting, the material is severely strained in the vicinity of the cutting edge, with high deformation rates (as high as 10^4-10^5 1/s) and a steep temperature gradient (heating and cooling rates exceeding 10^6 K/s) [68]. Strain magnitudes in the range of 2–4 are widely reported for deformation in the primary shear zones (in absence of shear localisation phenomenon where higher values are reported [69]), whereas shear strains as high as 25 are observed in secondary shear zones adjacent to the rake face of the tools [70]. The material deformation and the amount of generated heat largely depend on the tribological conditions on the tool-chip-workpiece surfaces, the tool geometry, and the cutting conditions [64,71]. The rates with which the dislocations evolve or annihilate depend on their interactions with the immobile dislocations, vacancies, grain boundaries and the lattice obstacles. The dislocation-annihilation mechanisms, such as recovery by glide and cross-slip as well as the remobilization of dislocations by vacancy climb [45,72], can lead to significant material softening effects during metal cutting. The high temperature and strain rates largely influence the concentration of vacancies and thus the dislocation annihilation process [73]. Hence, the stress contribution associated with the long-range lattice disturbances of immobile dislocations would, at least partly, be nullified in the shear zones. In addition, the precipitates may be fully or partially dissolved under such extreme (although non-equilibrium) conditions, resulting in no or limited precipitation-hardening effects in the shear zones. These arguments would only partly explain the limited differences observed in the cutting forces when machining the wrought and LB-PBF materials, and still cannot explain the reasons for the higher forces observed when machining EB-PBF materials. Therefore, two additional factors should be considered here: texture, and the extent of material work-hardening prior to the onset of crack formation during material removal.

Fig. 19 shows the chip-formation characteristics for wrought, LB-PBF and EB-PBF materials in as-received or as built conditions and after heat treatment. In the wrought material, cracks were observed more frequently after heat treatment compared to in the as-received condition on the edge of chips. A large density of deep cracks was observed in the LB-PBF material in both conditions. The chips formed after machining EB-PBF in as-built condition showed a large density of shallow cracks on the outer surface. A more profound crack formation was observed on edge of chips – corresponding to the location of maximum depth of cut – when machining heat-treated EB-PBF material.

The strong [001]//BD texture of the EB-PBF materials would influence the resistance to shear deformations occurring during the chip-formation process. The dislocation glide occurs on the planes with the highest density of atoms and towards the direction of the shortest lattice vectors [74]. Hence, the slip by dislocation glide in face-centred-cubic metals is favoured within the twelve octahedral $\{111\}\langle 110 >$ slip system. The slip becomes dominant on a crystallographic plane (belonging to the slip system) where the Schmid factor (SF) is highest [74]. The Schmid factor for the slip systems in polycrystalline materials can be obtained as $SF = cos\varphi cos\lambda$, where φ is the angle between the loading direction and the slip direction and λ is the angle between the slip plane normal and the loading direction, here predominantly the shear direction in the cutting process. The texture influences the value of SF and thus the associated ability for plastic deformation [75], and can explain the large anisotropic flow-stress properties commonly observed in EB-PBF materials [44]. It should be noted here that the cross slip of screw dislocations onto the {001} planes was also reported during

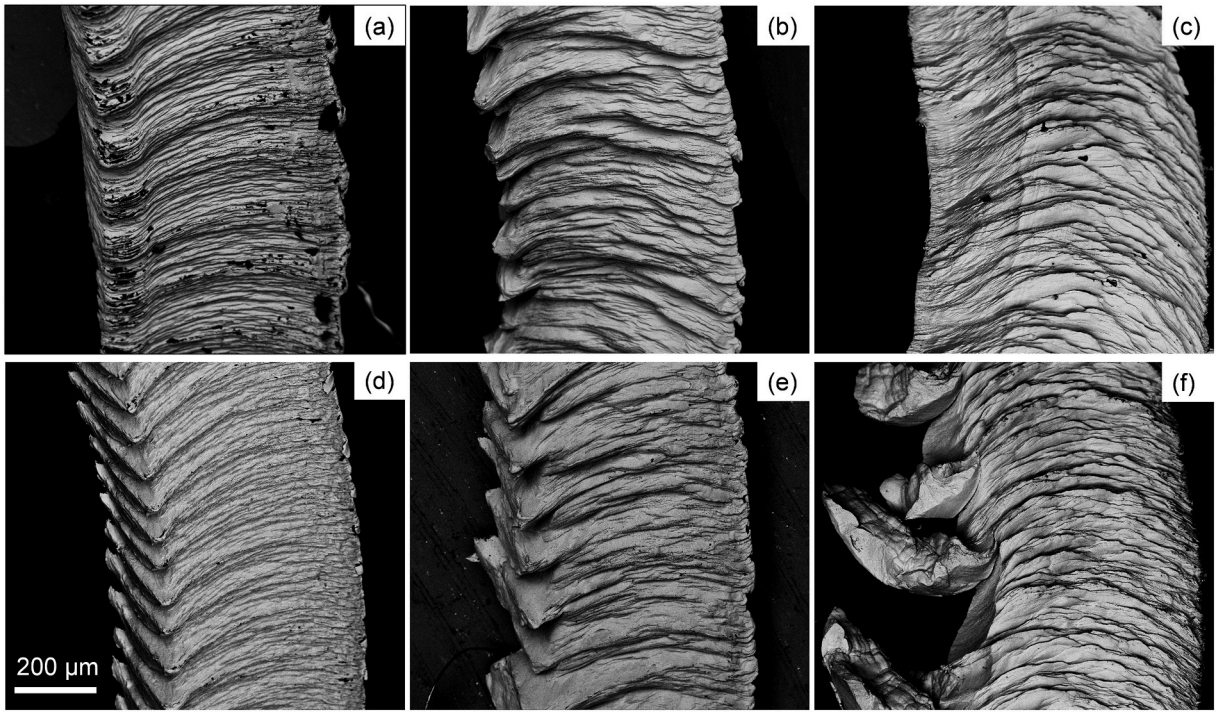

Fig. 19. Chip formation characteristics when machining wrought (a and d), LB-PBF (b and e), and EB-PBF (c and f) materials in as-received or as-built conditions, and after solutionising and aging treatment, respectively.

deformation of Alloy 718 [76]. Hence, an extended analysis of the texture effects on plastic deformation demands a-priori knowledge of the loading direction in machining and should, in principal, include the twelve octahedral and the additional 6 cubic $\{001\}\langle 110 >$ glide systems. Nevertheless, the strong [001]//BD texture is likely one of the major reasons for the higher forces observed when machining EB-PBF materials.

The extent of material work-hardening prior to the onset of crack formation during the chip separation process is the other important factor to be considered when evaluating the effects of microstructures on the thermo-mechanical loads during cutting. The chip-separation process essentially involves the crack propagation in front of the cutting edge [77]. The plastic energy dissipation at the crack front in ductile fracture depends on the yield strength of material, the strain-hardening (work-hardening) rate ($d\sigma/d\varepsilon$), the shear modulus, and the value of SF [46]. The rate with which the dislocations evolve and annihilate defines the strain-hardening rate and thus influences the onset of crack formation and its propagation rate during the chip-formation process. This would explain the observations in this study and those of Hagberg and Malm [67]. The onset of fracture for the LB-PBF material with a higher density of GNDs would occur earlier than that of the wrought materials, as is also implied from the chips shown in Fig. 19a–b and 19 d-e. In other words, the high density of GNDs in the LB-PBF material would lead to faster supersaturation of dislocations (and vacancies) during shear deformation, which in turn can result in lower work-hardening rates and lower fracture strains compared to those of wrought materials. These define the amount of plastic work (W) and therefore the amount of heat generated during machining. This implies that the heat generation during cutting cannot be simply correlated to the cutting forces. Instead, the deformation path, rate of work-hardening and onset of fracture during chip formation should all be considered for the estimation of heat generation during cutting [77]. Based on these arguments, among as-built and as-received materials, higher heat generation is expected when machining EB-PBF material, followed by wrought material. The amount of generated heat should be higher when machining EB-PBF material after solutionising and aging treatment compared to those of other materials.

It is, however, worth stressing here that the large anisotropic characteristics of additively manufactured materials – associated with differences in preferred crystallographic orientation, shape and distribution of grains as well as density of grain boundaries in build and transverse directions (c.f. Figs. 5 and 6 and the results summarised in Table 1) – would result in different deformation behaviour (and thus heat generations) depending on machining direction with respect to build direction, range of cutting conditions and tool geometry. In line with this hypothesis, the recent investigations on machining Alloy 718 and CoCrMo fabricated using LB-PBF method showed that the cutting forces can vary depending on the density of grain boundaries and the preferred crystallographic orientation of grains on the plane of cutting [78,79]. The range of cutting conditions and tool geometry predominately define the chip flow direction i.e. the direction of shear deformation on the rake surface with respect to the preferred crystallographic orientation and grain alignment in build direction. Hence, different contributions of hardening and recovery mechanisms would be expected during chip formation process. Consequently, the amount of heat generation and tool wear evolution rate can vary as those parameters change.

4.3. Tool wear mechanisms

In machining, different thermally- and mechanically-induced wear mechanisms are active on the tool surfaces, depending on the range of cutting conditions and the properties of the workpiece and tool materials. The flank and notch wear measurements presented in Fig. 13 showed distinct differences in wear rates when machining as-built or as-received materials. As discussed in Section 4.2, a higher heat generation is expected on a tool surface when machining the EB-PBF material. This leads to more pronounced thermally activated wear mechanisms on the tool surfaces when machining EB-PBF material, leading to larger flank and notch wear. Additionally, the amount, type and distribution of carbides, nitrides and oxides in the workpiece materials can influence the wear by abrasion [3,80]. Wrought material contained the largest amount of (Nb,Ti) (C,N) abrasive particles, whereas the EB-PBF material was comprised of a large amount of Al-rich oxides and a smaller amount of (Nb,Ti) (C,N). The hot-hardness values collected from published results [3,80] prove that these abrasive carbo-nitrides and oxides can potentially abrade WC-Co, controlling the rate of wear by abrasion. Apart from the amount of abrasive particles, their size distributions would also play a decisive role, as shown by Halila et al. [81]. Hence, the largest abrasion effect is expected for the wrought material, followed by the EB-PBF material. The detailed analysis of the wear surfaces, before and after etching (Figs. 14 and 16), showed chipping and spalling of the cutting-tool material on the rake surfaces. However, this effect was larger when machining EB-PBF and wrought materials, regardless of the state of the material (as-built or heat-treated conditions). This suggests that adhesion also plays a significant role in machining Alloy 718. The extreme shear stresses at relatively high temperatures provoke the separation of the tool material by adhesion, as shown in Fig. 18. The combined effects of these thermally- and mechanically-induced mechanisms determine the overall wear rates, as shown in Fig. 13, which is in agreement with previous findings [2,82,83]. The other mechanism that can potentially influence the rate of wear by abrasion is oxidation of Al-rich precipitates (or the γ matrix itself) at relatively high temperatures. As shown in Fig. 17, traces of Al-rich oxide fragments or layers were observed (mainly) on the flank wear lands after removal of the adhered materials when using HCl etchant. The presence of these oxide layers or fragments in the wrought and LB-PBF materials, with no or limited amounts of oxide inclusions in the workpieces, suggests that they formed and deposited due to oxidation of Al-rich precipitates or the γ phase itself. These Al-rich oxides may have a higher hardness than the tool material (WC–Co), and hence can contribute to wear by abrasion [80,84]. Naturally, higher heat generation increases the amount of these oxide fragments, leading to higher wear by abrasion. This is likely an additional reason for the increased wear rate observed when machining LB-PBF material in heat-treated condition.

The complex tribological interactions between the tool and the workpiece materials demand a fundamental understanding of the material deformation behaviour during cutting as well as a fair knowledge on the relative contributions of the thermally- and mechanically-induced wear mechanisms. This means that the descriptive methodologies – based solely on the macro properties such as ductility, strength (obtained using uniaxial tensile or compression tests), and hardness – do not necessarily lead to reliable machinability assessments. This can clearly be observed by comparing the hardness values in Fig. 11 and the tool wear results presented in Fig. 13. While the higher hardness of EB-PBF material in as-built condition would explain the higher wear rates when machining this material compared to the LB-PBF and wrought materials under as-built and as-received conditions, it cannot explain the differences observed between wear rate when machining LB-PBF and wrought materials (lower wear rates observed when machining LB-PBF material with higher bulk hardness in as-built condition). A detailed computational and experimental analysis is required for machinability assessment of additively manufactured materials with more complex microstructural characteristics compared to the wrought materials. This remains to be investigated in the future.

5. Conclusions

A detailed characterisation of the wrought and additively manufactured materials using LB-PBF and EB-PBF technologies showed significantly different microstructural characteristics in terms of: a) grain size distribution; b) type, size and amount of micro-constituents; c) Kernel

Average Misorientation (KAM); and d) preferred crystallographic orientation (texture). The combined effects of these distinctive characteristics led to a large difference in tool wear when machining Alloy 718 fabricated using various manufacturing methods. The major observations can be summarised as follows:

- The texture and the extent of material work-hardening prior to the onset of crack formation during material removal can significantly influence the cutting forces and the heat generation in cutting process. The strong [001]//BD texture in EB-PBF material likely leads to a larger barrier-hardening effect compared to LB-PBF and wrought materials. In addition, higher energies would be required for activating the slip systems in strongly textured materials under given loading conditions, contributing to higher heat generations and larger cutting forces. The influence texture could be evaluated using Schmid Factor. The extent of work-hardening prior to the onset of crack formation is not only related to the texture itself, but also the mount and size of γ' and γ'' precipitates, grain size distribution and other long-range interactions influencing the rates with which the dislocations evolve and annihilate.
- A large density of GNDs in LB-PBF material likely result in faster supersaturation of dislocation and vacancies and thus lower work-hardening rates and lower fracture strains. The effects of both mechanisms are reflected in measured cutting forces, where the largest force was observed when machining EB-PBF material, regardless of whether it was in as-built or heat-treated condition.
- Higher heat generation is expected when machining EB-PBF material due to its resistance to deformation caused by strong [001]//BD texture and larger work-hardening prior to chip removal. Hence, thermally-induced wear mechanisms are believed to play a more significant role when machining this material in as-built and heat-treated condition.
- Abrasion is believed to have the largest effect when machining wrought Alloy 718, comprising a large amount of hard, Nb-rich carbides and Ti-rich carbo-nitrides. Al-rich oxide layers (or fragments) were observed on the flank surface of the tools when machining wrought and additively manufactured Alloy 718 in as-received or as-built conditions and after heat treatment. These oxide layers likely contribute to wear by abrasion, the effects of which are believed to be larger when machining additively manufactured Alloy 718.
- While the dislocation-based description of flow-stress properties can explain the relationship between microstructural characteristics and hardness, additional factors should be included when describing the material-deformation behaviour in metal cutting. This is because the severe plastic deformation at large strain rates and steep temperature gradients provokes different hardening and softening (recovery) phenomena, which largely differ from those occurring in hardness or (standard iso-thermal) uniaxial tensile tests. Hence, the hardness or tensile properties should be used with caution when comparing the machinability of workpiece materials, even when comparing a certain alloy fabricated using different technologies and different thermal treatments. The physics-based methodology presented in this study opens new opportunities for assessing the machinability of an arbitrary alloy regardless of the manufacturing method and thermal-deformation histories.

Author contribution

Amir Malakizadi: Writing - Original Draft, Supervision, Conceptualization, Methodology, Software, Formal analysis, Investigation, Data Curation, Visualization, Project administration, Tina Hajali: Writing - Review & Editing, Methodology, Investigation, Data Curation, Fiona Schulz: Writing - Review & Editing, Supervision, Methodology, Investigation, Stefan Cedergren: Writing - Review & Editing, Methodology, Resources, Joakim Ålgårdh: Writing - Review & Editing, Methodology, Resources, Rachid M'Saoubi: Writing - Review & Editing, Methodology, Resources, Eduard Hryha: Writing - Review & Editing, Methodology, Resources, Funding acquisition, Peter Krajnik: Writing - Review & Editing, Methodology, Resources, Funding acquisition.

Declaration of competing interest

The authors declare that they have no known competing financial interests or personal relationships that could have appeared to influence the work reported in this paper.

Acknowledgments

This work was conducted within framework of collaboration between Centre for Metal Cutting Research (MCR) and Centre for Additive Manufacturing – Metal (CAM2) at Chalmers University of Technology, the latter supported by the Swedish Governmental Agency of Innovation Systems (Vinnova).

References

[1] L.L. Parimi, M.M. Attallah, J. Gebelin, R.C. Reed, E.S. Huron, R.C. Reed, M. C. Hardy, M.J. Mills, R.E. Montero, P.D. Portella, J. Telesman, Direct laser fabrication of inconel-718: effects on distortion and microstructure, Superalloys 12 (2012) 511–519.
[2] A. Bhatt, H. Attia, R. Vargas, V. Thomson, Wear mechanisms of WC coated and uncoated tools in finish turning of Inconel 718, Tribol. Int. 43 (5) (2010) 1113–1121.
[3] P. Hoier, A. Malakizadi, P. Stuppa, S. Cedergren, U. Klement, Microstructural characteristics of Alloy 718 and Waspaloy and their influence on flank wear during turning, Wear 400–401 (2018) 184–193.
[4] S. Olovsjö, L. Nyborg, Influence of microstructure on wear behaviour of uncoated WC tools in turning of Alloy 718 and Waspaloy, Wear 282–283 (2012) 12–21.
[5] B. Wang, et al., Advancements in material removal mechanism and surface integrity of high speed metal cutting: a review, Int. J. Mach. Tool Manufact. 166 (2021) 103744.
[6] W. Grzesik, P. Niesłony, W. Habrat, J. Sieniawski, P. Laskowski, Investigation of tool wear in the turning of Inconel 718 superalloy in terms of process performance and productivity enhancement, Tribol. Int. 118 (2018) 337–346.
[7] V. Bushlya, J. Zhou, P. Avdovic, J.-E. Ståhl, Performance and wear mechanisms of whisker-reinforced alumina, coated and uncoated PCBN tools when high-speed turning aged Inconel 718, Int. J. Adv. Manuf. Technol. 66 (2013) 9–12.
[8] V. Bushlya, et al., Tool wear mechanisms of PcBN in machining Inconel 718: analysis across multiple length scale, CIRP Annals (2021).
[9] C. Darshan, S. Jain, M. Dogra, M.K. Gupta, M. Mia, Machinability improvement in Inconel-718 by enhanced tribological and thermal environment using textured tool, J. Therm. Anal. Calorim. 138 (1) (2019) 273–285.
[10] N. Tamil Alagan, P. Zeman, P. Hoier, T. Beno, U. Klement, Investigation of micro-textured cutting tools used for face turning of alloy 718 with high-pressure cooling, J. Manuf. Process. 37 (2019) 606–616.
[11] N. Tamil Alagan, P. Hoier, T. Beno, U. Klement, A. Wretland, Coolant boiling and cavitation wear – a new tool wear mechanism on WC tools in machining Alloy 718 with high-pressure coolant, Wear 452–453 (2020) 203284.
[12] N. Tamil Alagan, P. Hoier, P. Zeman, U. Klement, T. Beno, A. Wretland, Effects of high-pressure cooling in the flank and rake faces of WC tool on the tool wear mechanism and process conditions in turning of alloy 718, Wear 434–435 (2019) 102922.
[13] Y. Kaynak, Evaluation of machining performance in cryogenic machining of Inconel 718 and comparison with dry and MQL machining, Int. J. Adv. Manuf. Technol. 72 (5) (2014) 919–933.
[14] F. Pušavec, J. Kopač, Sustainability assessment: cryogenic machining of Inconel 718, Strojniški vestnik-Journal of Mechanical Engineering 57 (9) (2011) 637–647.
[15] P. Sivaiah, V. Ajay Kumar, M. Singh, H. Kumar, Effect of novel hybrid texture tool on turning process performance in MQL machining of Inconel 718 superalloy, Mater. Manuf. Process. 35 (1) (2020/01/02 2020) 61–71.
[16] Z. Yang, L. Zhu, G. Zhang, C. Ni, B. Lin, Review of ultrasonic vibration-assisted machining in advanced materials, Int. J. Mach. Tool Manufact. 156 (2020) 103594.
[17] Z. Shang, Z. Liao, J.A. Sarasua, J. Billingham, D. Axinte, On modelling of laser assisted machining: forward and inverse problems for heat placement control, Int. J. Mach. Tool Manufact. 138 (2019) 36–50.
[18] S. Cedergren, S. Olovsjö, G. Sjöberg, L. Nyborg, The effects of grain size and feed rate on notch wear and burr formation in wrought Alloy 718, in: English), the International Journal of Advanced Manufacturing Technology vol. 67, 2013, pp. 1501–1507, 5–8.
[19] S. Olovsjö, A. Wretland, G. Sjöberg, The effect of grain size and hardness of wrought Alloy 718 on the wear of cemented carbide tools, Wear 268 (9–10) (2010) 1045–1052.
[20] C. Furusho, Y. Kousai, M. Osaki, K. Uno, Development of new alloy 718 with super machinability. Proceedings of the 9th International Symposium on Superalloy 718

& Derivatives: Energy, Aerospace, and Industrial Applications, Springer, 2018, pp. 1073–1085.
[21] S. Olovsjö, P. Hammersberg, P. Avdovic, J.-E. Ståhl, L. Nyborg, Methodology for evaluating effects of material characteristics on machinability—theory and statistics-based modelling applied on Alloy 718, Int. J. Adv. Manuf. Technol. 59 (1–4) (2012) 55–66.
[22] P. Avdovic, L. Xu, M. Andersson, J.-E. Ståhl, Evaluating the machinability of Inconel 718 using polar diagrams, J. Eng. Gas Turbines Power 133 (7) (2011), 072101-072101-7.
[23] M.K. Thompson, et al., Design for additive manufacturing: trends, opportunities, considerations, and constraints, CIRP Annals 65 (2) (2016) 737–760.
[24] T. DebRoy, et al., Additive manufacturing of metallic components – process, structure and properties, Prog. Mater. Sci. 92 (2018) 112–224.
[25] S. Sanchez, et al., Powder Bed Fusion of nickel-based superalloys: a review, Int. J. Mach. Tool Manufact. 165 (2021) 103729.
[26] L. Chen, Q. Xu, Y. Liu, G. Cai, J. Liu, Machinability of the laser additively manufactured Inconel 718 superalloy in turning, Int. J. Adv. Manuf. Technol. 114 (3) (2021) 871–882.
[27] E. Ducroux, G. Fromentin, F. Viprey, D. Prat, A. D'Acunto, New mechanistic cutting force model for milling additive manufactured Inconel 718 considering effects of tool wear evolution and actual tool geometry, J. Manuf. Process. 64 (2021) 67–80.
[28] F. Careri, D. Umbrello, K. Essa, M.M. Attallah, S. Imbrogno, The effect of the heat treatments on the tool wear of hybrid Additive Manufacturing of IN718, Wear 470–471 (2021) 203617.
[29] E. Hosseini, V.A. Popovich, A review of mechanical properties of additively manufactured Inconel 718, Additive Manufacturing 30 (2019) 100877.
[30] C. Pauzon, A. Raza, E. Hryha, P. Forêt, Oxygen balance during laser powder bed fusion of Alloy 718, Mater. Des. 201 (2021) 109511.
[31] S. Goel, K. Bourreau, J. Olsson, U. Klement, S. Joshi, Can appropriate thermal post-treatment make defect content in as-built electron beam additively manufactured alloy 718 irrelevant? Materials 13 (3) (2020) 536.
[32] S.-H. Sun, et al., Electron beam additive manufacturing of Inconel 718 alloy rods: impact of build direction on microstructure and high-temperature tensile properties, Additive Manufacturing 23 (2018) 457–470.
[33] T. Gundgire, S. Goel, U. Klement, S. Joshi, Response of different electron beam melting produced Alloy 718 microstructures to thermal post-treatments, Mater. Char. 167 (2020) 110498.
[34] R. Jiang, A. Mostafaei, J. Pauza, C. Kantzos, A.D. Rollett, Varied heat treatments and properties of laser powder bed printed Inconel 718, Mater. Sci. Eng., A 755 (2019) 170–180.
[35] H.Y. Wan, Z.J. Zhou, C.P. Li, G.F. Chen, G.P. Zhang, Effect of scanning strategy on grain structure and crystallographic texture of Inconel 718 processed by selective laser melting, J. Mater. Sci. Technol. 34 (10) (2018) 1799–1804.
[36] S. Holland, X. Wang, X.Y. Fang, Y.B. Guo, F. Yan, L. Li, Grain boundary network evolution in Inconel 718 from selective laser melting to heat treatment, Mater. Sci. Eng., A 725 (2018) 406–418.
[37] C. Pei, D. Shi, H. Yuan, H. Li, Assessment of mechanical properties and fatigue performance of a selective laser melted nickel-base superalloy Inconel 718, Mater. Sci. Eng., A 759 (2019) 278–287.
[38] R. Bergmann, R. Chan, R. Hielscher, J. Persch, G. Steidl, Restoration of Manifold-Valued Images by Half-Quadratic Minimization, arXiv: Numerical Analysis, 2015.
[39] EM Fayed, M Saadati, D Shahriari, V Brailovski, M Jahazi, M Medraj, Optimization of the post-process heat treatment of Inconel 718 superalloy fabricated by laser powder bed fusion process, Metals 11 (1) (2021 Jan) 144.
[40] M.R. Bache, C. Coleman, M.P. Coleman, V. Gray, C. Boettcher, Microstructure evolution in flow formed IN 718 products and subsequent fatigue crack growth properties, Fatig. Fract. Eng. Mater. Struct. 41 (11) (2018) 2249–2258.
[41] J.Z.S. Li, J. Yang, Q. Deng, J. Du, X. Xie, B. Li, Z. o Xu, Z. Cao, Z. Su, C. Jiang, The effect of phase on crack propagation under creep and fatigue conditions in alloy 718, in: Superalloys 718, 625, 706 and Various Derivatives (1994), The Minerals, Metals & Materials Society, 1994, pp. 545–555.
[42] D. Deng, R.L. Peng, H. Brodin, J. Moverare, Microstructure and mechanical properties of Inconel 718 produced by selective laser melting: sample orientation dependence and effects of post heat treatments, Mater. Sci. Eng., A 713 (2018) 294–306.
[43] M.M. Kirka, F. Medina, R. Dehoff, A. Okello, Mechanical behavior of post-processed Inconel 718 manufactured through the electron beam melting process, Mater. Sci. Eng., A 680 (2017) 338–346.
[44] D. Deng, J. Moverare, R.L. Peng, H. Söderberg, Microstructure and anisotropic mechanical properties of EBM manufactured Inconel 718 and effects of post heat treatments, Mater. Sci. Eng., A 693 (2017) 151–163.
[45] M. Fisk, J.C. Ion, L.-E. Lindgren, Flow stress model for IN718 accounting for evolution of strengthening precipitates during thermal treatment, Comput. Mater. Sci. 82 (2014) 531–539.
[46] J.W. Kysar, Energy dissipation mechanisms in ductile fracture, J. Mech. Phys. Solid. 51 (5) (2003) 795–824.
[47] P. Zhang, S.X. Li, Z.F. Zhang, General relationship between strength and hardness, Mater. Sci. Eng., A 529 (2011) 62–73.
[48] D. Tabor, The Hardness of Metals, Oxford university press, 2000.
[49] A. Malmelöv, M. Fisk, A. Lundbäck, L.-E. Lindgren, Mechanism based flow stress model for alloy 625 and alloy 718, Materials 13 (24) (2020) 5620.
[50] M.R. Ahmadi, et al., Modeling of precipitation strengthening in Inconel 718 including non-sphericalγ″ precipitates, Model. Simulat. Mater. Sci. Eng. 25 (5) (2017), 055005.
[51] E.I. Galindo-Nava, L.D. Connor, C.M.F. Rae, On the prediction of the yield stress of unimodal and multimodal γ′ Nickel-base superalloys, Acta Mater. 98 (2015) 377–390.
[52] R. Armstrong, The influence of polycrystal grain size on several mechanical properties of materials, Metall. Mater. Trans. B 1 (5) (1970) 1169–1176.
[53] O. Gokcekaya, T. Ishimoto, S. Hibino, J. Yasutomi, T. Narushima, T. Nakano, Unique crystallographic texture formation in Inconel 718 by laser powder bed fusion and its effect on mechanical anisotropy, Acta Mater. 212 (2021) 116876.
[54] T. Johnston, C. Feltner, Grain size effects in the strain hardening of polycrystals, Metall. Mater. Trans. B 1 (5) (1970) 1161.
[55] L. Remy, The interaction between slip and twinning systems and the influence of twinning on the mechanical behavior of fcc metals and alloys, Metallurgical Transactions A 12 (3) (1981) 387–408.
[56] M. Ashby, The deformation of plastically non-homogeneous materials, Philos. Mag. A: A Journal of Theoretical Experimental and Applied Physics 21 (170) (1970) 399–424.
[57] A.J. Schwartz, M. Kumar, B.L. Adams, D.P. Field, Electron Backscatter Diffraction in Materials Science, Springer, 2009.
[58] C. Moussa, M. Bernacki, R. Besnard, N. Bozzolo, About quantitative EBSD analysis of deformation and recovery substructures in pure Tantalum, in: IOP Conference Series: Materials Science and Engineering vol. 89, IOP Publishing, 2015, 012038, 1.
[59] A.P. Zhilyaev, I. Shakhova, A. Belyakov, R. Kaibyshev, T.G. Langdon, Wear resistance and electroconductivity in copper processed by severe plastic deformation, Wear 305 (1) (2013) 89–99.
[60] M. Al-Saadi, F. Sandberg, P.G. Jönsson, C.N. Hulme-Smith, Modelling of strengthening mechanisms in wrought nickel-based 825 alloy subjected to solution annealing, Metals 11 (5) (2021) 771.
[61] G.I. Taylor, H. Quinney, The latent energy remaining in a metal after cold working, Proc. R. Soc. Lond. - Ser. A Contain. Pap. a Math. Phys. Character 143 (849) (1934) 307–326.
[62] P. Knysh, Y.P. Korkolis, Determination of the fraction of plastic work converted into heat in metals, Mech. Mater. 86 (2015) 71–80.
[63] T. Augspurger, B. Peng, F. Klocke, B. Döbbeler, Heat flow into the tool in cutting super alloy Inconel 718, J. Mech. Eng. Autom. 8 (2018) 1–8.
[64] W. Grzesik, Advanced Machining Processes of Metallic Materials- Theory, Modelling and Application, Elsevier, Netherlands, 2008.
[65] J.C. Garcia-Gonzalez, W. Moscoso-Kingsley, V. Madhavan, Tool rake face temperature distribution when machining Ti6Al4V and Inconel 718, Procedia Manufacturing 5 (2016) 1369–1381.
[66] Y. Liu, M. Agmell, D. Xu, A. Ahadi, J.-E. Stahl, J. Zhou, Numerical contribution to segmented chip effect on residual stress distribution in orthogonal cutting of Inconel718, Int. J. Adv. Manuf. Technol. 109 (3) (2020) 993–1005.
[67] A. Hagberg, P. Malm, Material Deformation Mechanisms during Machining of Superalloys, Chalmers University of Technology, 2010.
[68] A. la Monaca, D.A. Axinte, Z. Liao, R. M'Saoubi, M.C. Hardy, Towards understanding the thermal history of microstructural surface deformation when cutting a next generation powder metallurgy nickel-base superalloy, Int. J. Mach. Tool Manufact. (2021) 103765.
[69] J. Johansson, C. Persson, H. Lai, M. Hörnqvist Colliander, Microstructural examination of shear localisation during high strain rate deformation of Alloy 718, Mater. Sci. Eng., A 662 (2016) 363–372.
[70] D. Sagapuram, et al., On the cutting of metals: a mechanics viewpoint, J. Manuf. Sci. Eng. 142 (11) (2020).
[71] E.M. Trent, P.K. Wright, Metal Cutting, Butterworth-Heinemann, Boston, 2000.
[72] Y. Bergström, H. Hallén, An improved dislocation model for the stress-strain behaviour of polycrystalline α-Fe, Mater. Sci. Eng. 55 (1) (1982) 49–61.
[73] M. Militzer, W.P. Sun, J.J. Jonas, Modelling the effect of deformation-induced vacancies on segregation and precipitation, Acta Metall. Mater. 42 (1) (1994) 133–141.
[74] D. Hull, D.J. Bacon, Introduction to Dislocations, Elsevier, 2011.
[75] H. Touazine, K. Chadha, M. Jahazi, P. Bocher, Characterization of subsurface microstructural alterations induced by hard turning of Inconel 718, J. Mater. Eng. Perform. 28 (11) (2019) 7016–7024.
[76] S. Ghorbanpour, et al., A crystal plasticity model incorporating the effects of precipitates in superalloys: application to tensile, compressive, and cyclic deformation of Inconel 718, Int. J. Plast. 99 (2017) 162–185.
[77] V.P. Astakhov, Tribology of Metal Cutting, in: Tribology and Interface Engineering), 1 ed., Elsevier Science, 2006.
[78] J.D. Pérez-Ruiz, L.N.L. de Lacalle, G. Urbikain, O. Pereira, S. Martínez, J. Bris, On the relationship between cutting forces and anisotropy features in the milling of LPBF Inconel 718 for near net shape parts, Int. J. Mach. Tool Manufact. 170 (2021) 103801.
[79] P. Fernandez-Zelaia, V. Nguyen, H. Zhang, A. Kumar, S.N. Melkote, The effects of material anisotropy on secondary processing of additively manufactured CoCrMo, Additive Manufacturing 29 (2019) 100764.
[80] P. Hoier, A. Malakizadi, U. Klement, P. Krajnik, Characterization of abrasion- and dissolution-induced tool wear in machining, Wear 426–427 (2019) 1548–1562.
[81] F. Halila, C. Czarnota, M. Nouari, Analytical stochastic modeling and experimental investigation on abrasive wear when turning difficult to cut materials, Wear 302 (1) (2013) 1145–1157.

[82] S. Cedergren, S. Olovsjö, G. Sjöberg, L. Nyborg, The effects of grain size and feed rate on notch wear and burr formation in wrought Alloy 718, Int. J. Adv. Manuf. Technol. 67 (5) (2013) 1501–1507.
[83] M. Rakesh, S. Datta, Effects of cutting speed on chip characteristics and tool wear mechanisms during dry machining of Inconel 718 using uncoated WC tool, Arabian J. Sci. Eng. 44 (9) (2019) 7423–7440.
[84] P. Hoier, A. Malakizadi, S. Friebe, U. Klement, P. Krajnik, Microstructural variations in 316L austenitic stainless steel and their influence on tool wear in machining, Wear 428–429 (2019) 315–327.